Chapter 7

Experimental Results

7.1 Images

The experimental results of this research are based on real range images obtained from the CESAR lab at Oak Ridge National Laboratory. These images, as well as the intensity images, are developed using a Perceptron laser range finder [25]. The Perceptron database has 40 real range images. In addition, the experimentation of edge detection involved a set of synthetic images containing objects having curved surfaces. The Perceptron real images have a size of 512×512 and quantization of 12 bits. The synthetic images, which include curved objects, have a size of 240×240. Figures 7.1 and 7.2 show representative samples of Perceptron range images. These images contain single and multiple polyhedral objects. The registered intensity images for those samples depicted in Figures 7.1 and 7.2 are shown in Figures 7.3 and 7.4.

The object faces in the Perceptron range images were cut from large sheets of freshly pressed thick cardboard, and held together at the edges using standard wide masking tape (on both the inside and outside). Every possible precaution was taken to insure minimum deviations from planarity. The background of these images is planar surface and the wall is made from sheets of the same cardboard, also taped together at the edges. The floor is standard linoleum. The objects are roughly 1 m^3 in volume, while the scale of object vertices is in centimeters.

7.2 Results of Range Image Edge Detectors

This section illustrates the results of the proposed edge detection techniques presented in Chapter 4. These techniques, which were applied to the Perceptron real and synthetic images, are the FFT-based ring operator, difference in surface normal direction, and gradient direction using adaptive Gaussian. In addition, several well-known edge-detection methods are applied for the test images for comparison with the proposed methods. These methods are the Canny edge detector, the magnitude of the gradient as

obtained using the Sobel edge detector, and zero-crossings after filtering by the Laplacian-of-Gaussian operator (LoG).

Table 7.1 shows the parameters and threshold values used in the edge detection of the synthetic and real range images. The edge detectors use the small values of the parameters for the synthetic images and the large values for the real images. All images were smoothed before edge detection using the operator presented in Section 4.2.1.2.

Table 7.1 Parameters and threshold values used in the edge detection of the tested range images. ABSN is the angle between surface normals edge detector and GDAG is the gradient direction using adaptive Gaussian filter edge.

Edge Detector	Filter (window)Size(w)	Gaussian Width (σ)	Threshold Values (T)	Ring Length(L)
FFT			[1.5 – 120.0]	[32,64]
ABSN	[5×5 – 17×17]		[25.0 – 35.0]	
GDAG	[7×7 – 17×17]	[0.75 – 8.5]	[15.0 – 20.0]	
Canny		[1.5 – 8.5]	[0.0063–0.015]	
Sobel	[3×3]		[0.75 – 120.0]	
LoG	[5×5 – 17×17]	[0.75 –11.0]	[0.025 – 1.50]	

Figures 7.5-7.10 demonstrate results of the proposed edge detection methods for the real range images. Based on a subjective comparison, the gradient direction using adaptive Gaussian filter method performs better than the FFT-based ring operator and difference in surface normal direction in terms of finding roof edges, omitting false edges, and computation speed. Relative to the FFT-based ring operator, the difference of surface normals technique achieves good results in detecting roof edges, but the algorithm is much slower because of the need to perform cubic fitting over large windows. Meanwhile, the FFT-based method shows some deficiencies, primarily several spurious edge points and the absence of a few roof edges. The FFT-based method is also time intensive; however, this is acceptable because the motivation of this work is to provide edge information that

will facilitate image segmentation. Applying the proposed methods, both roof and step edges are detected efficiently. The thicker contours are produced due to the large windows for the edge operators. Moreover, these approaches share the common characteristic that they may obscure small object faces, which can be treated during segmentation. This is handled later using the thinning algorithm.

Figures 7.11-13 illustrate the results of the well-known methods. In this case, partial and complete absences of roof edges for the real range images are seen. The Canny method results are of particular interest due to that method's widespread use in edge detection [14]. Although for this method, different values for the parameters of variance and window size are evaluated in order to obtain acceptable results, partial absence of roof edges is still noticed. The thin contours do not help in the image segmentation in the further step.

Figures 7.14 and 7.15 present a representative sample of the edges that manually detected (ground truth) of the Perceptron database. These images provide an overall subjective comparison between all the results of methods of edge detection discussed above.

Synthetic images were tested for the purpose of evaluating the applicability of both the proposed and the well-known methods to images containing objects with curved surfaces.. The results, provided in Figure 7.16, show that the Sobel edge detector fails in detecting the roof edges in the curved object. The LoG method successfully identifies the edges but with less accuracy than all the proposed methods.

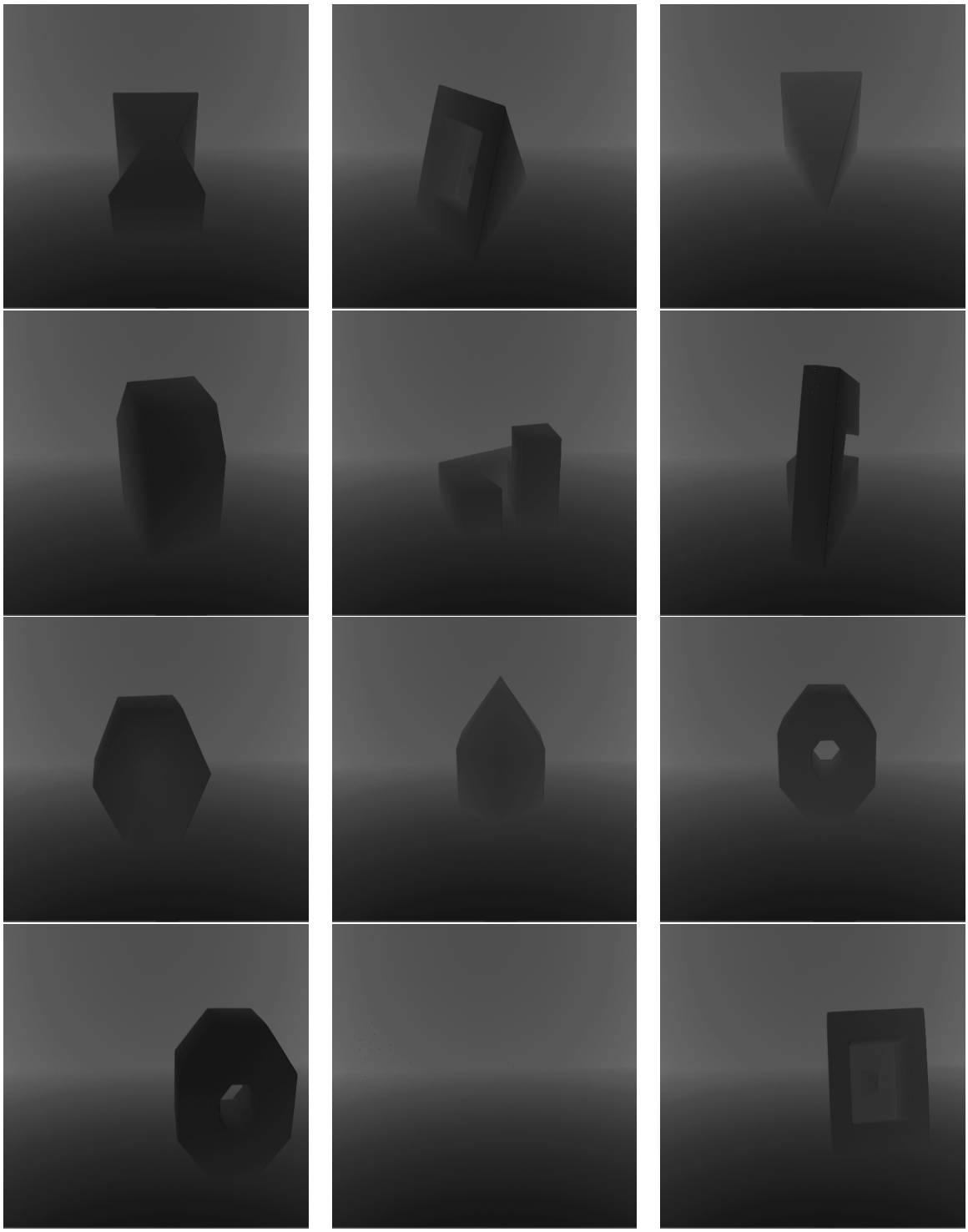

Figure 7.1 A representative sample of the real range images acquired using the Perceptron laser range finder (LRF). The images are of size 512×512 and are quantized of 12 bits per pixel. The images contain a single polyhedral object.

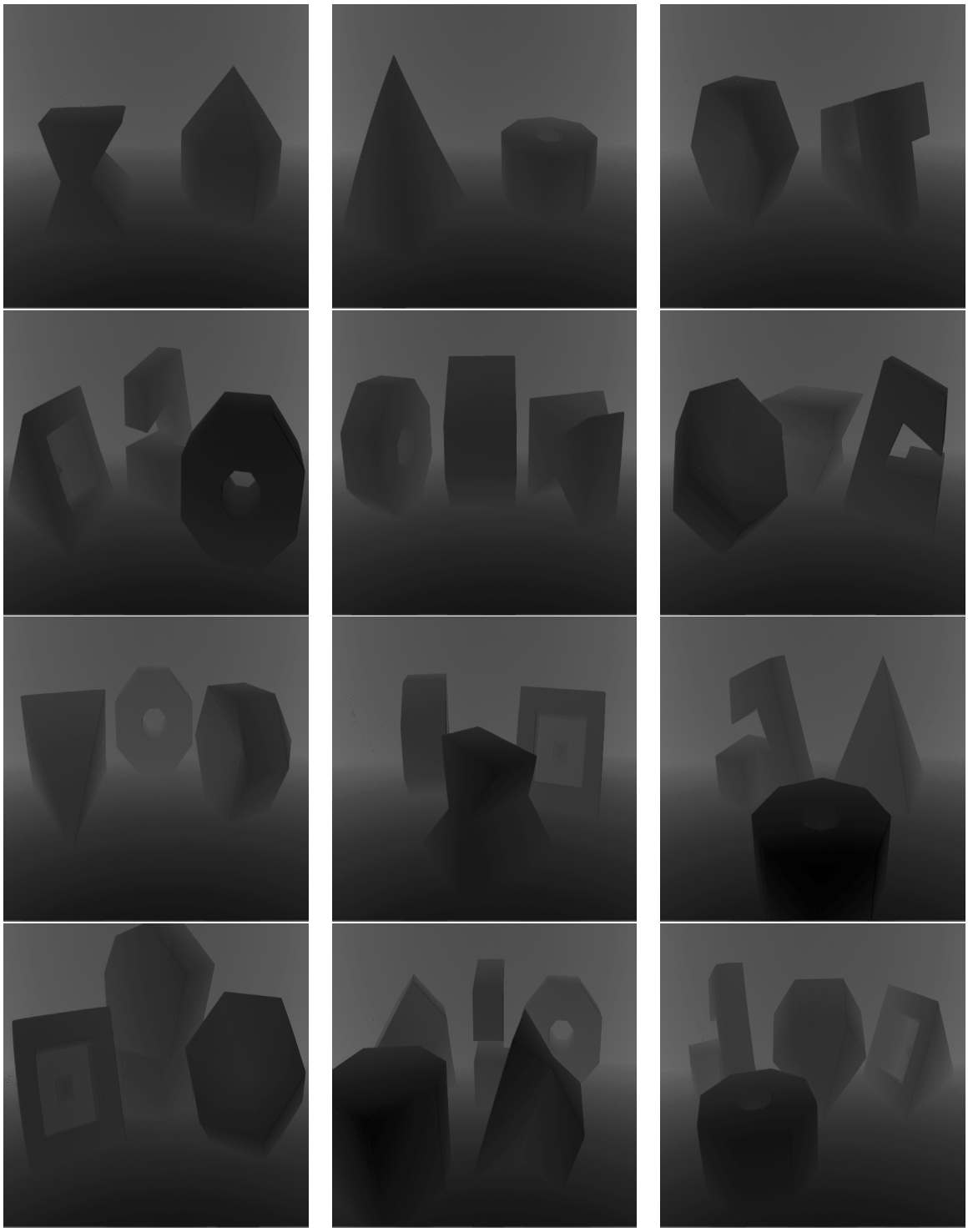

Figure 7.2 A representative sample of the real range images acquired using the Perceptron laser range finder (LRF). The images are of size 512×512 and are quantized of 12 bits per pixel. The images include non-overlapped and overlapped multiple polyhedral objects.

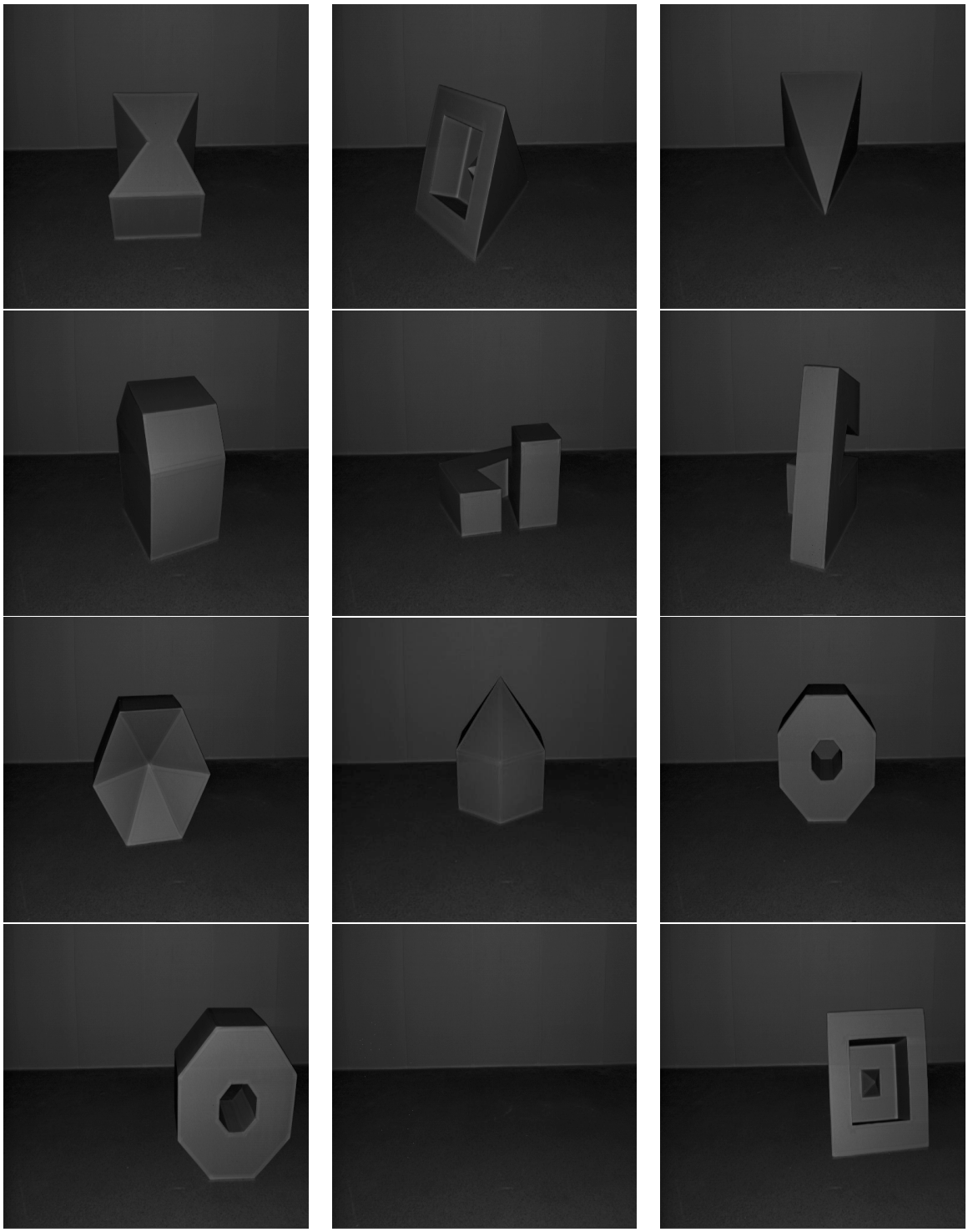

Figure 7.3 The registered reflectance images for those depicted in Figure 7.1. The images are of size 512×512 and contain a single polyhedral object. These images are not used in this work but they illustrate the difference between intensity and range images.

Figure 7.4 The registered reflectance images for those depicted in Figure 7.2. The images are size 512×512 and include non-overlapped and overlapped multiple polyhedral objects. These images are not used in this work but they illustrate the difference between intensity and range images.

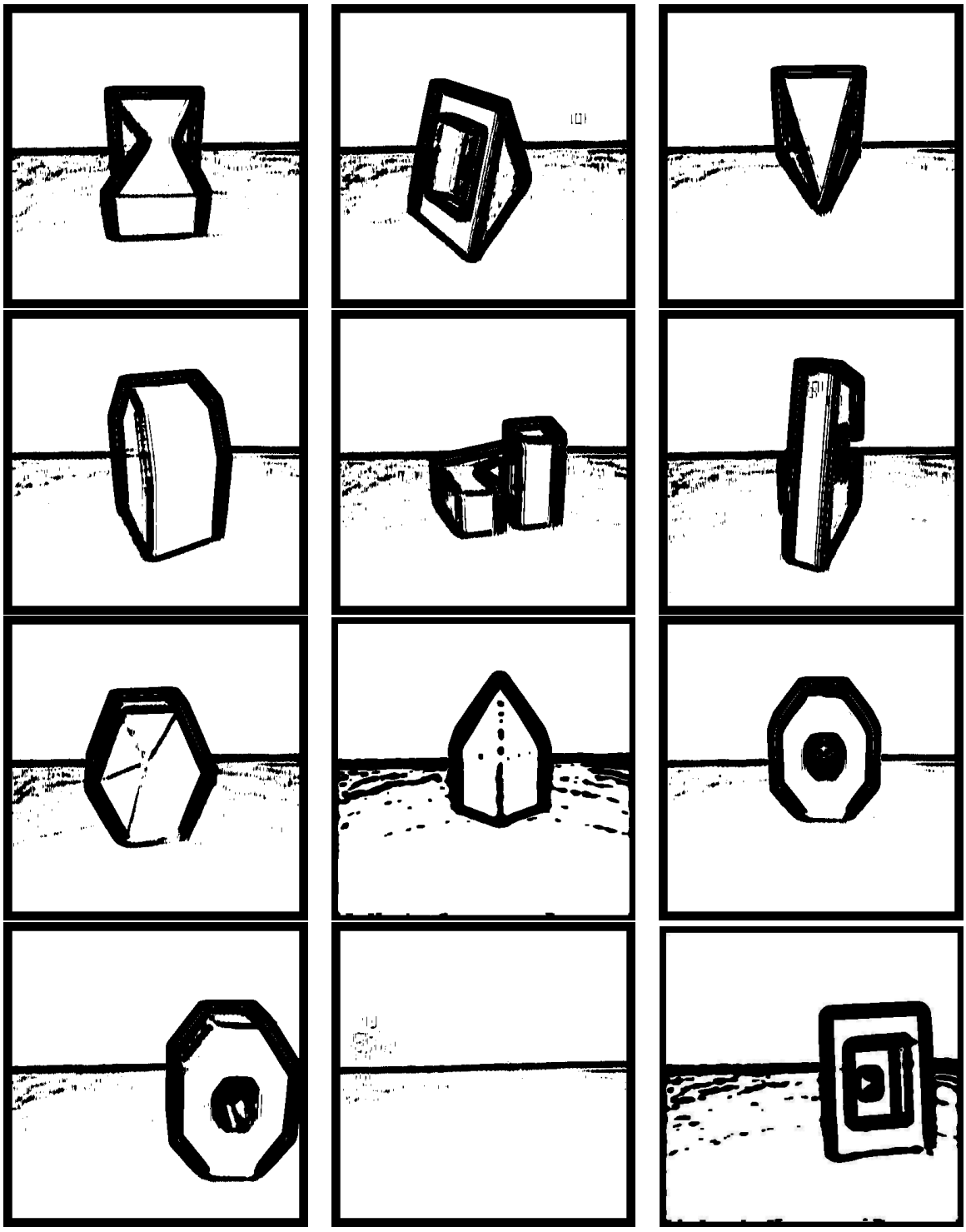

Figure 7.5 Results obtained by applying the noise reduction and FFT-based ring edge detector operators on the real range images in Figure 7.1. There are few roof edges are partially absent using this technique of edge detection.

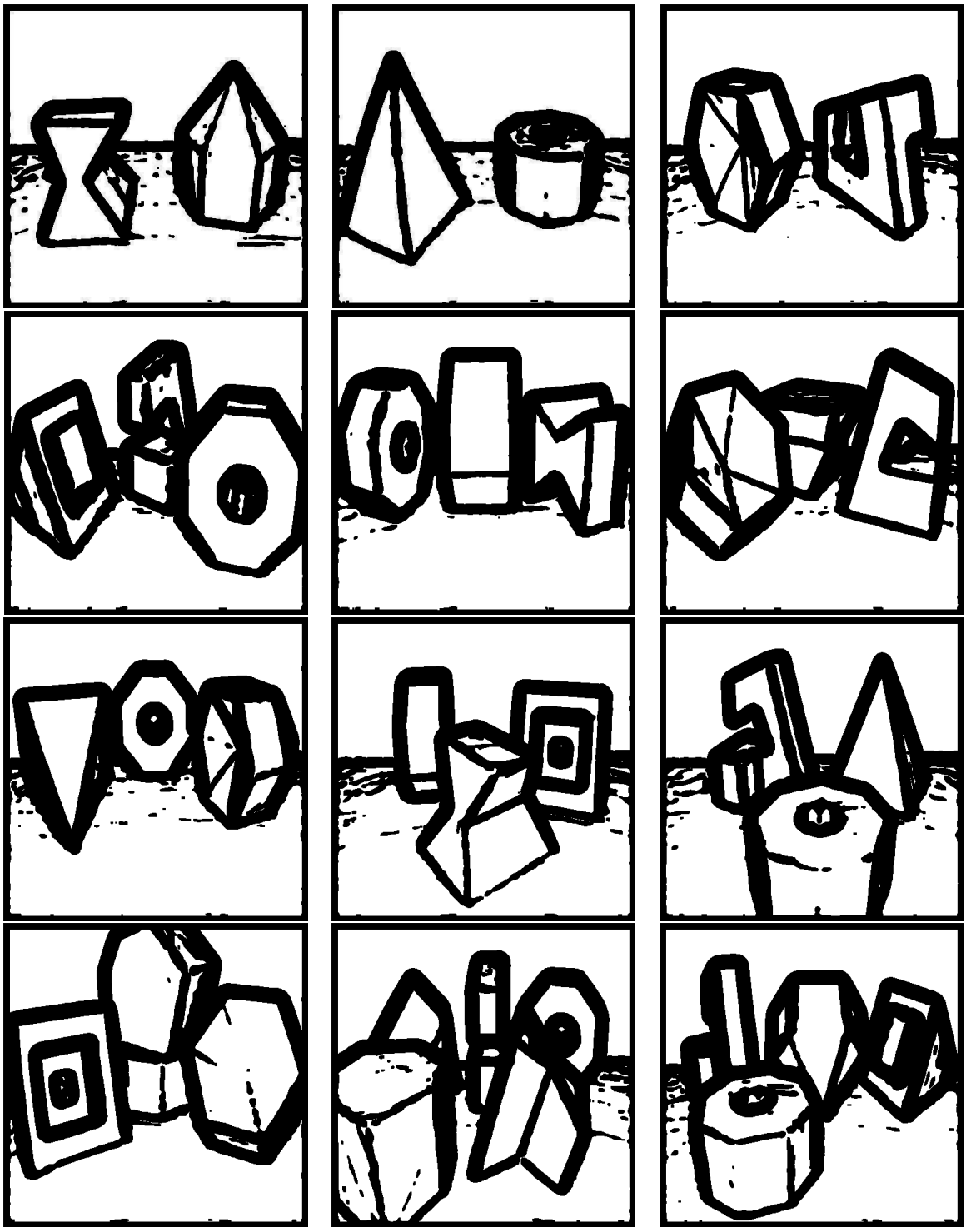

Figure 7.6 Results obtained by applying the noise reduction and the FFT-based ring edge detector operators on the real range images in Figure 7.2. The performance of this technique is good in the case of multiple overlapped objects.

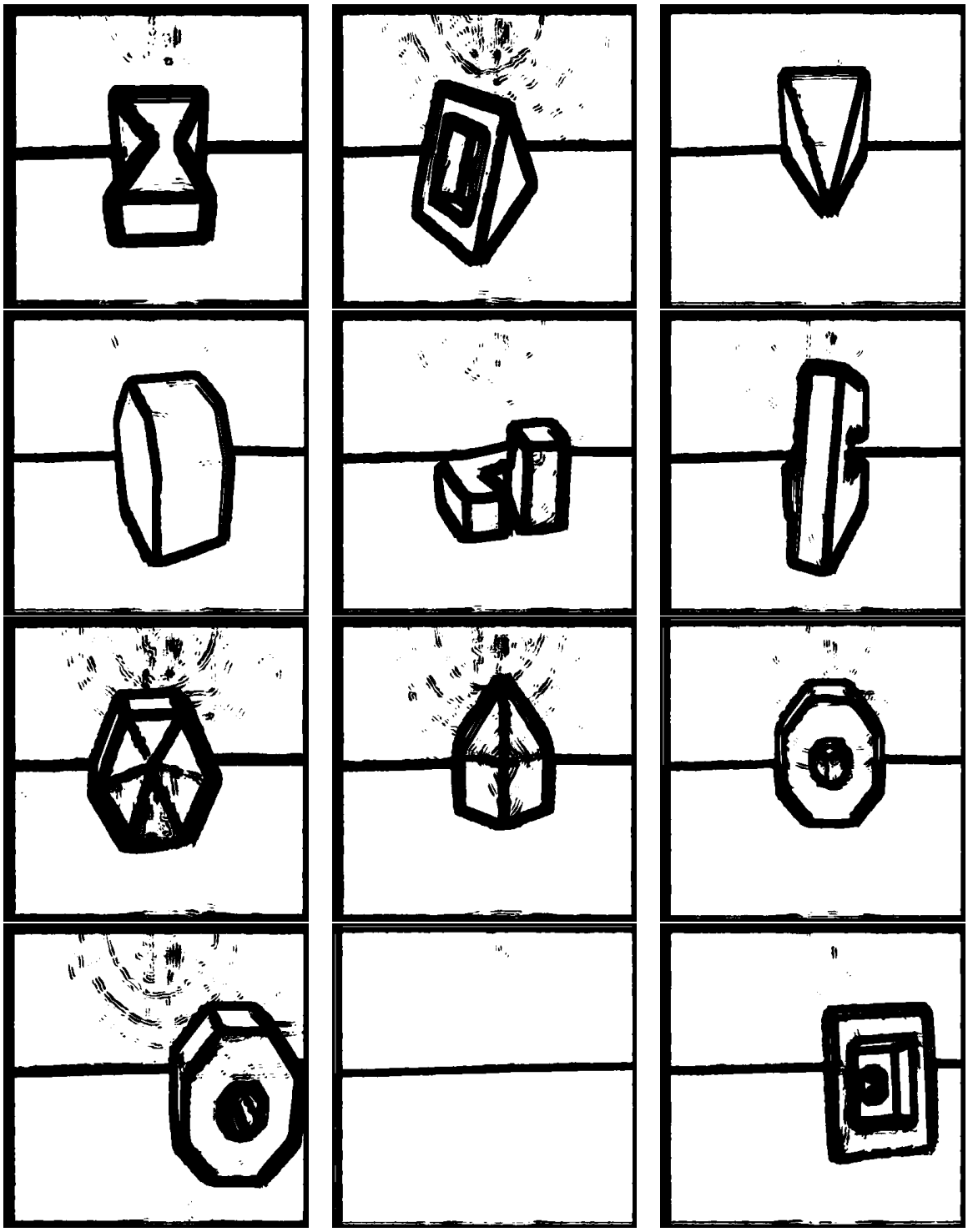

Figure 7.7 Results obtained by applying the noise reduction and the angle between surface normals edge detector operators on the real range images in Figure 7.1. This technique performs better than the FFT approach in terms of roof edge detection.

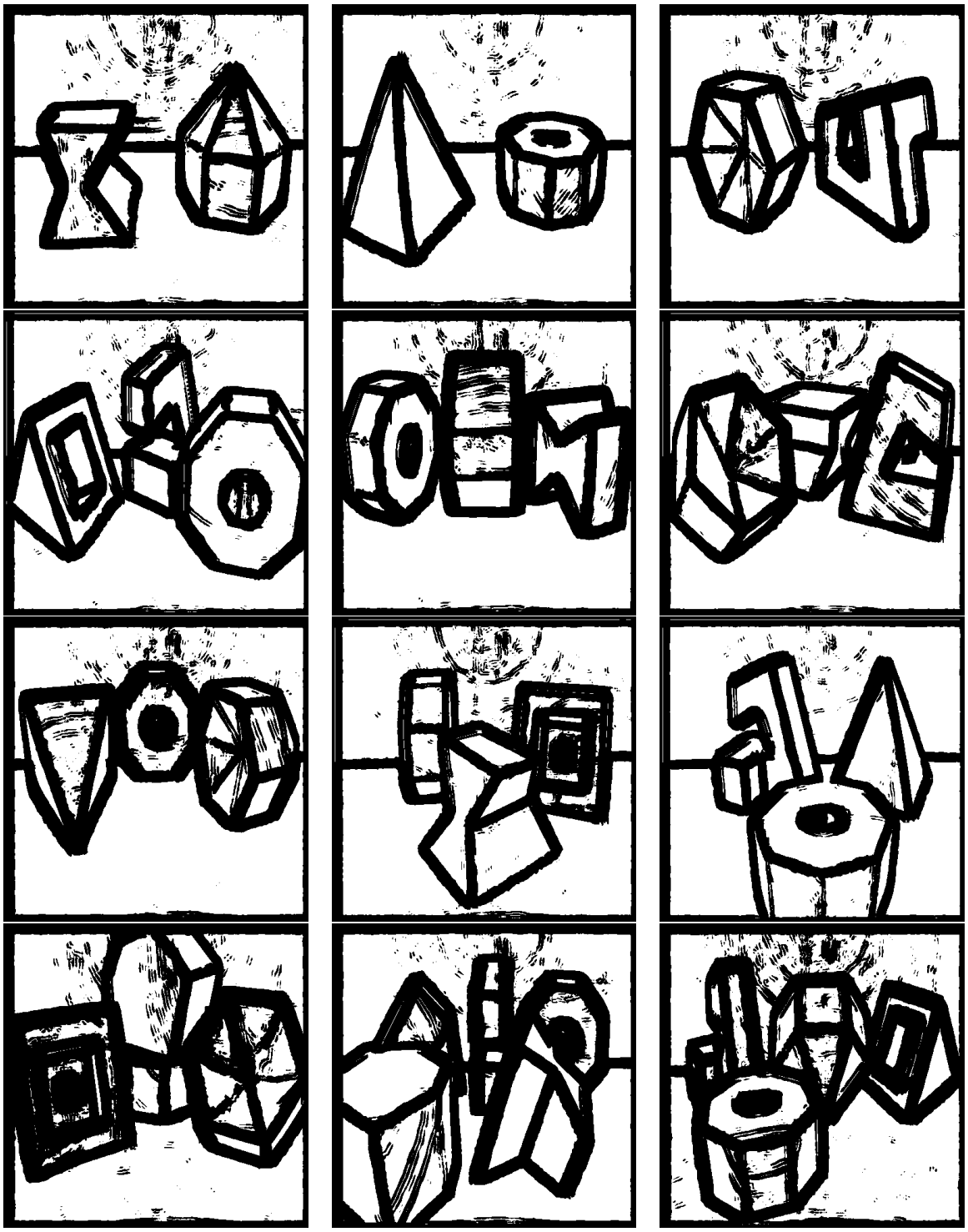

Figure 7.8 Results obtained by applying the noise reduction and the angle between surface normals edge detector operators on the real range images in Figure 7.2. To detect all roof edges noises appeared in the range image. It is considered as a thresholding issue.

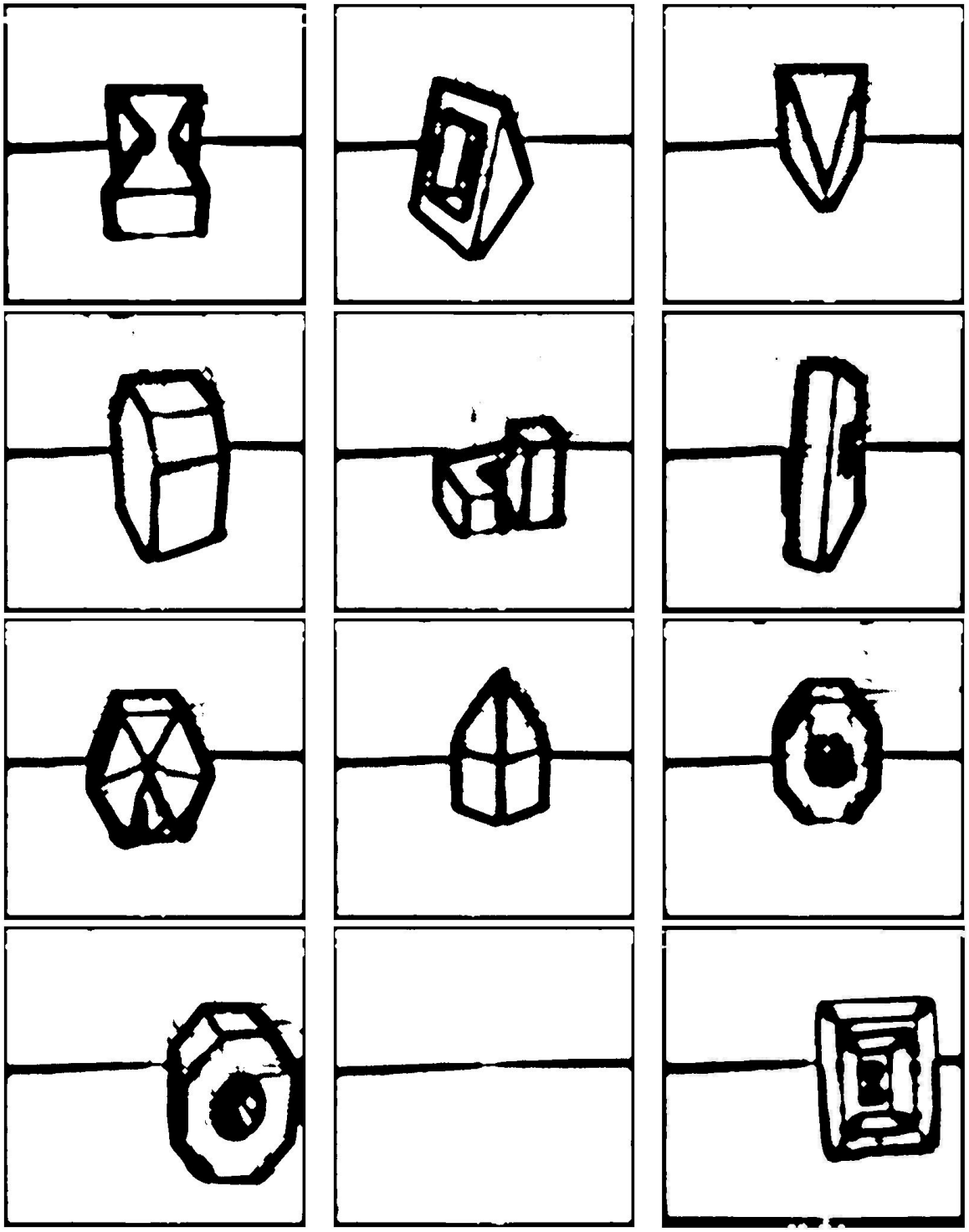

Figure 7.9 Results obtained by applying noise reduction and gradient direction using adaptive Gaussian filter edge detector operators on the real range images in Figure 7.1. Here, the results seem better than the other approach's in terms of presence of roof edges and absence of noise.

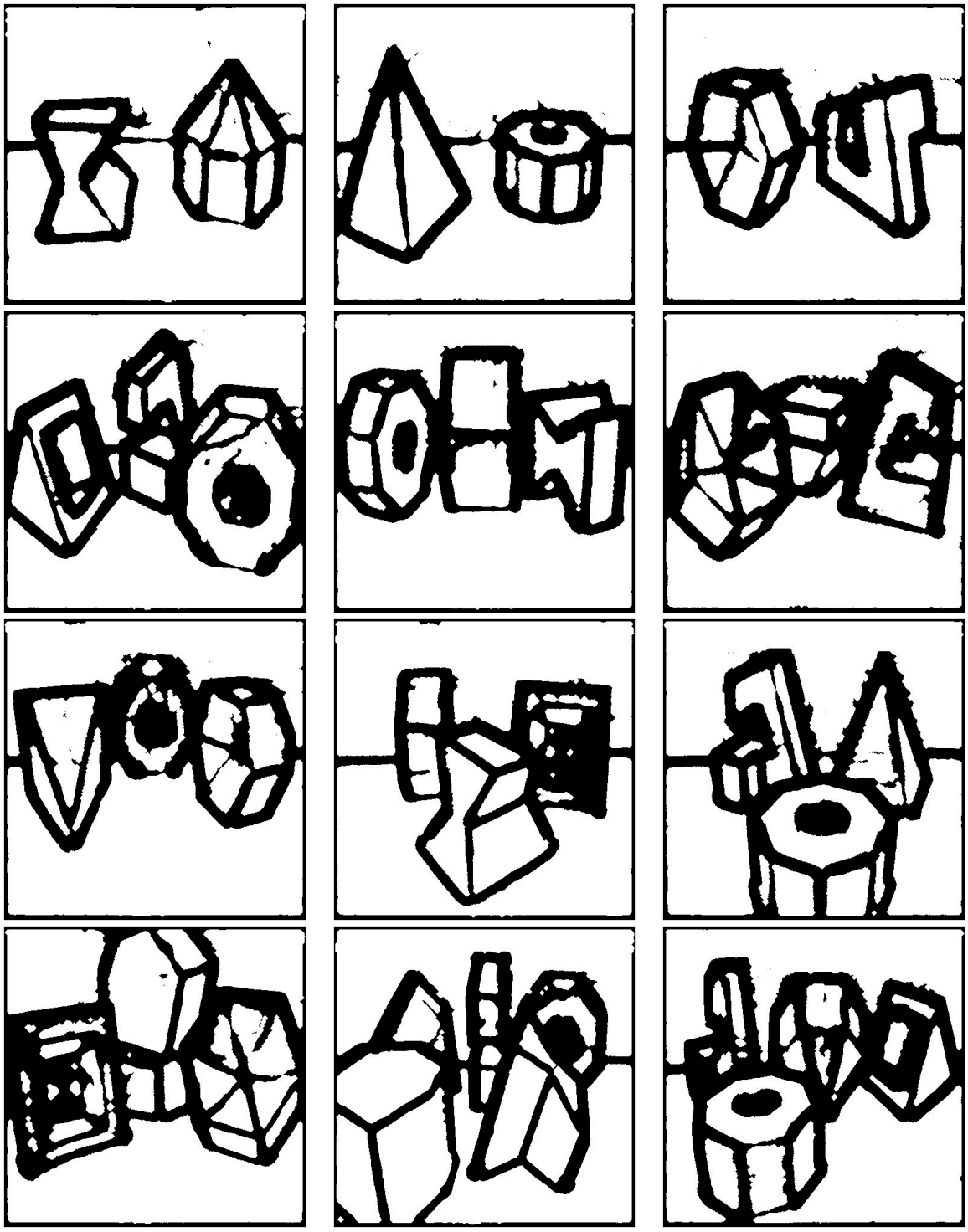

Figure 7.10 Results obtained by applying noise reduction and gradient direction using adaptive Gaussian filter edge detector operators on the real range images in Figure 7.2. The edge detector operator did not detect regions that have small sizes (less than minimum area size of a region to be detected).

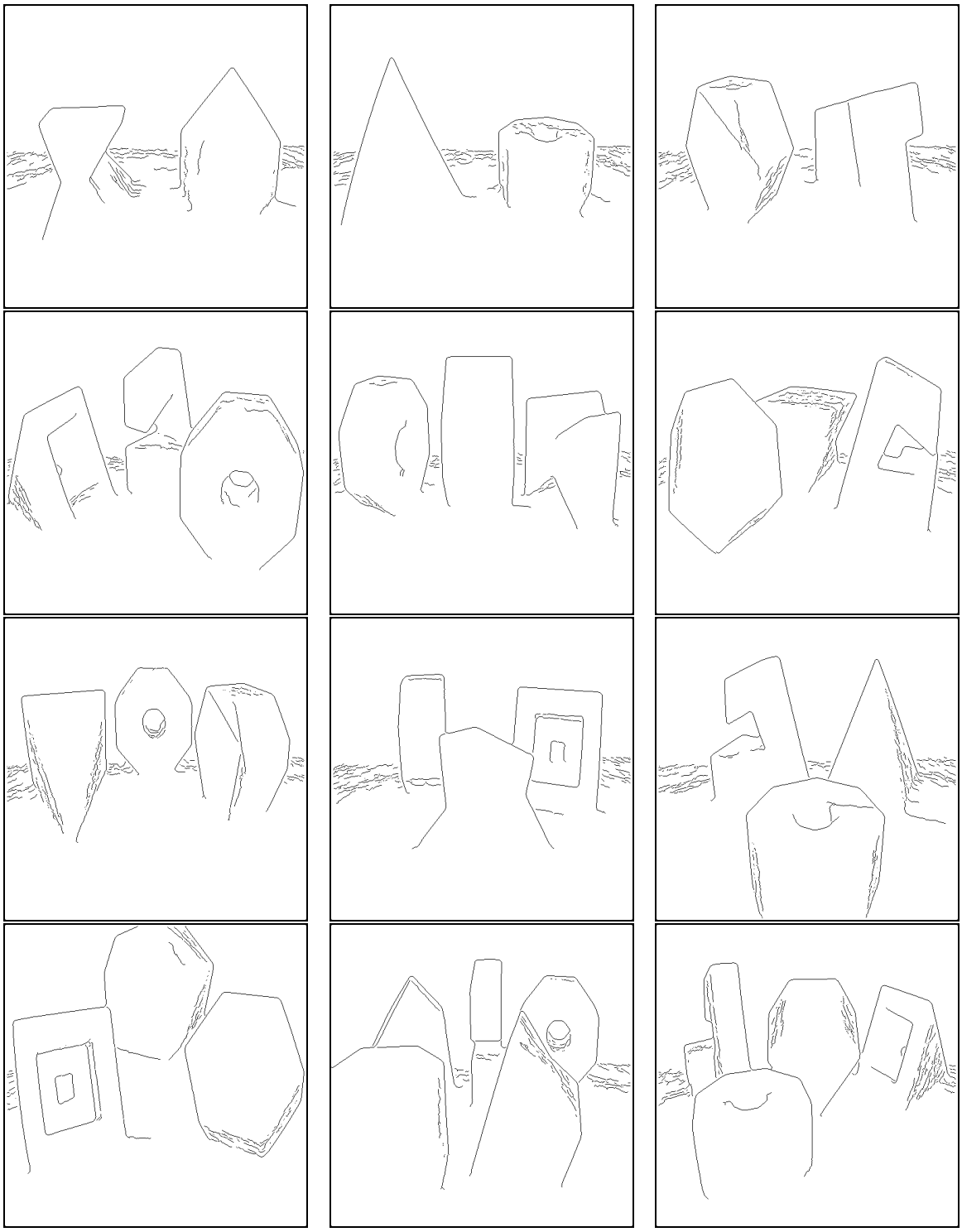

Figure 7.11 Results obtained by applying noise reduction Canny edge detector operators on the real range images in Figure 7.2. Partial and complete absence of the roof edges. This approach should be one of the best traditional techniques for edge detection.

Figure 7.12 Results obtained by applying the noise reduction and gradient method Sobel edge detector operators on the real range images in Figure 7.2. Complete absence of the roof edges and complete presence of jump edge.

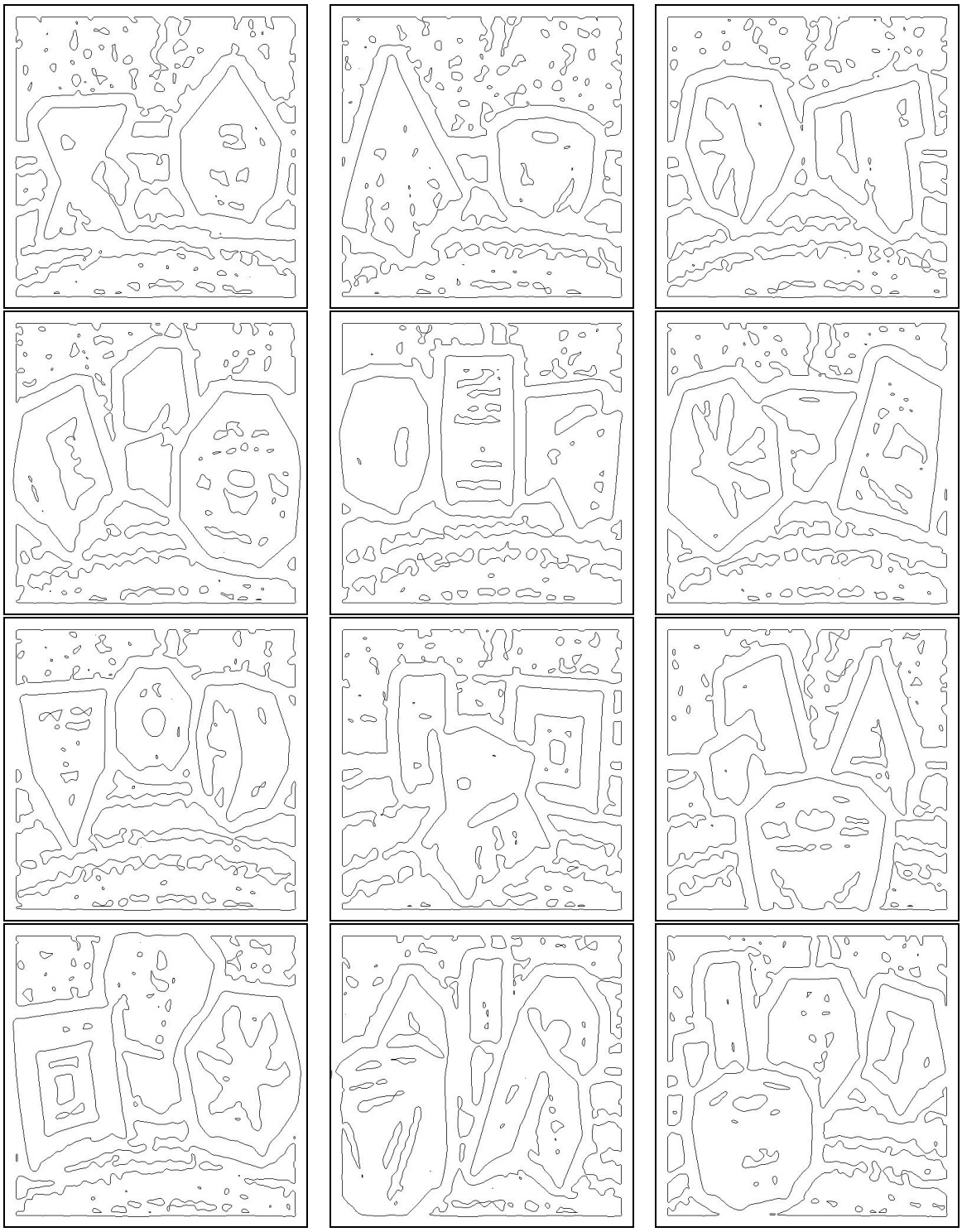

Figure 7.13 Results obtained by applying noise reduction operator and zero-crossings after filtering by the Laplacian-of-Gaussian operator (LoG) on the real range images in Figure 7.2. Complete and partial absence of roof edges and the contours are closed.

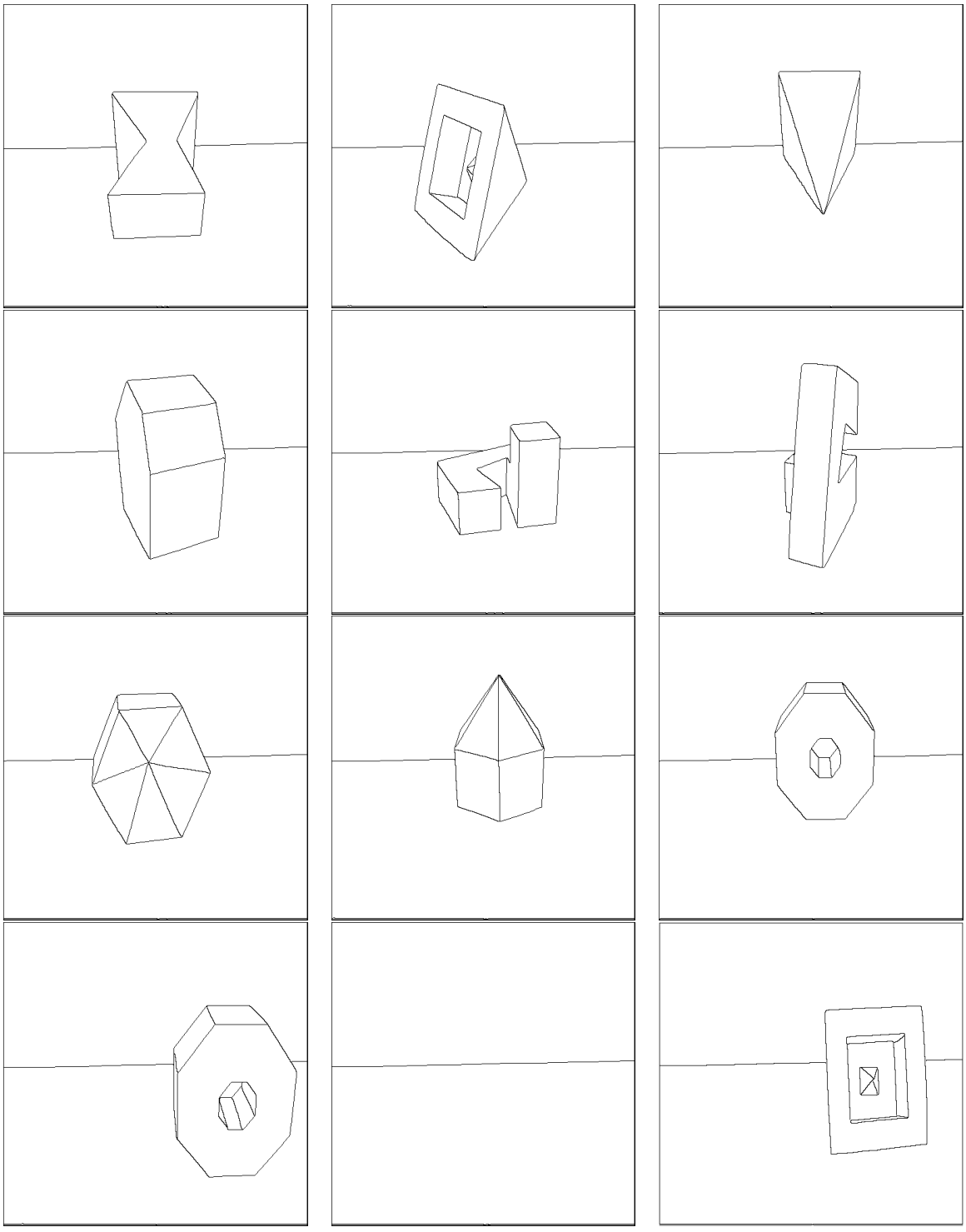

Figure 7.14 The ground truth edge maps of the real range images in Figure 7.1. These images are obtained from the ground truth segmented images of Figure 7.19.

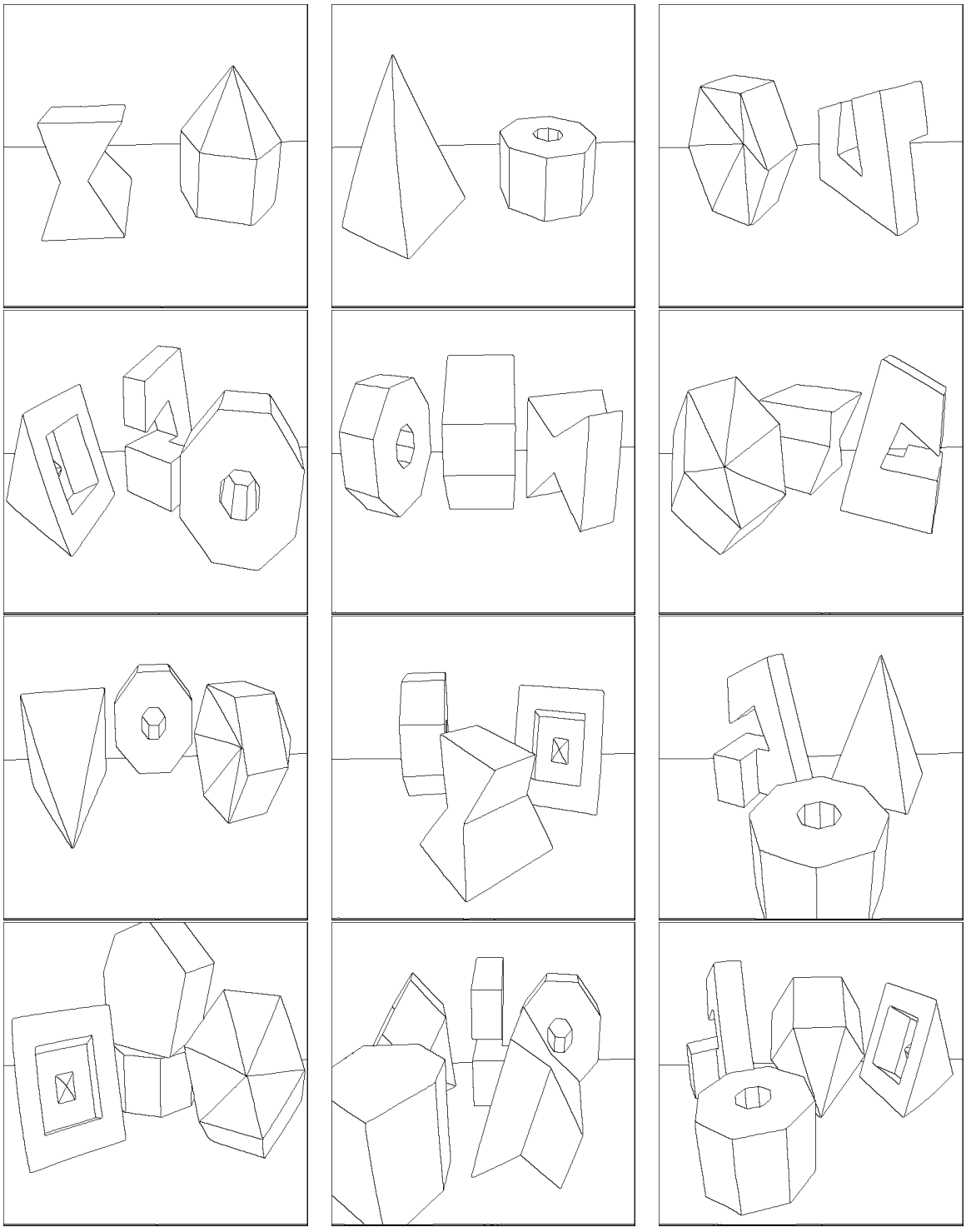

Figure 7.15 The ground truth edge maps of the real range images in Figure 7.2. These images are obtained from the ground truth segmented images of Figure 7.20.

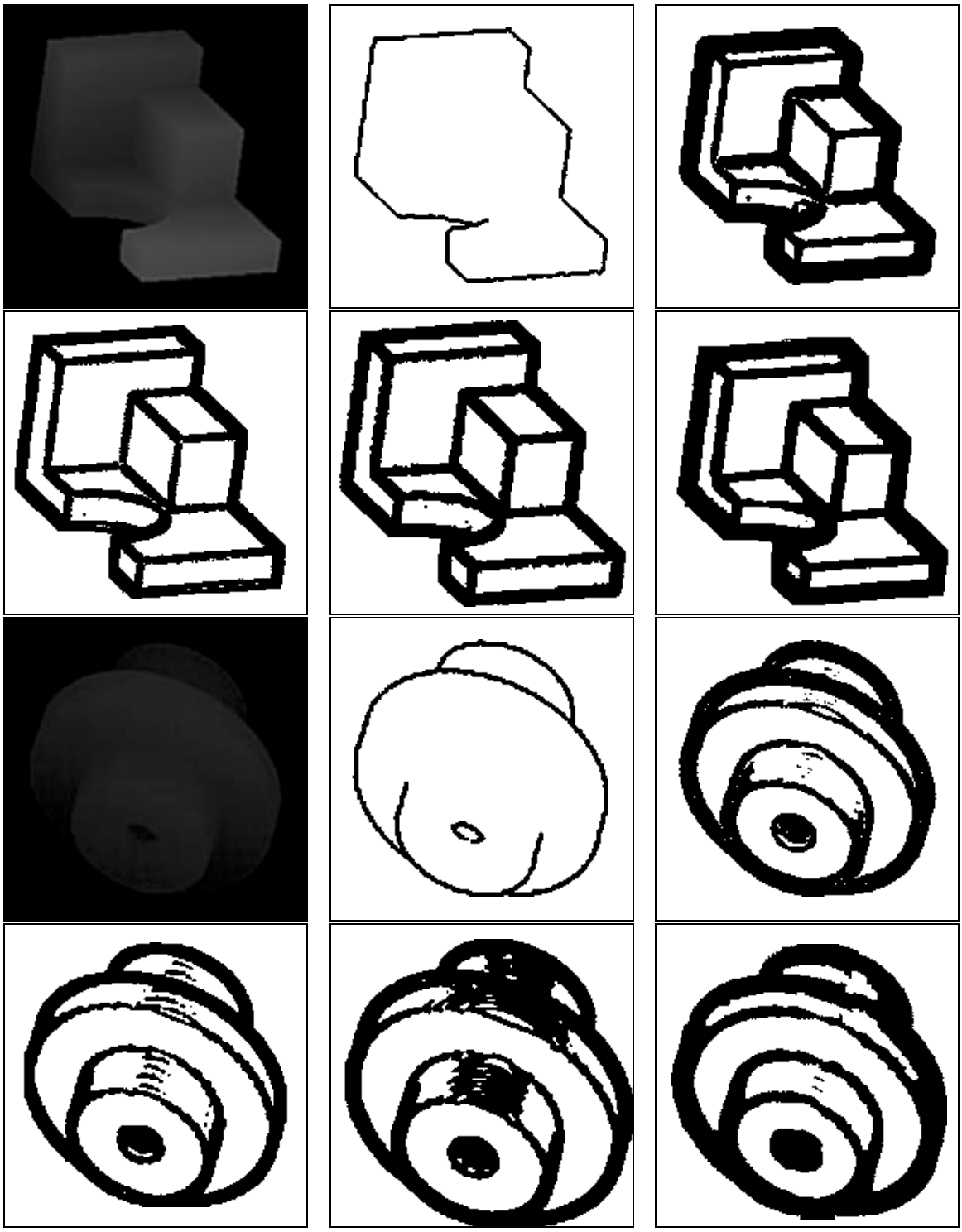

Figure 7.16 Results obtained by applying both common and proposed edge detectors on a representative sample of synthetic range images with curved surfaces. The common operators are Sobel, Laplacian of Gaussian (LoG), FFT-based ring operator, angle between surface normals operator, and gradient direction using adaptive Gaussian Filter operator respectively.

7.3 Results of Range Image Segmentation

In the previous section, it was identified that the gradient direction using adaptive Gaussian edge detector is the best among the methods evaluated; therefore, it is used in initial segmentation. The segmentation of range images occurs in two phases, as shown in Figure 4.1. The first phase is the initial segmentation, which includes smoothing, edge detection, thinning, connected component labeling, and region adjacency graph construction. The second phase is the segmentation refinement, which includes edge removal, removing small regions, successive split and merge, and region refinement. Table 7.2 shows the parameters and threshold values used in the refinement segmentation of the real range images.

Table 7.2 Parameters and threshold values used in the segmentation refinement.

Parameters	Values
Min. region size (pixels)	[100]
Max. point distance (cm)	[12.0,16.0]
Max. perpendicular distance (cm)	[4.0]
Splitting threshold (cm)	[0.6, 10.0]
Min angle between two regions to merge (degree)	[20 – 35]

The set of segmented images in Figure 7.17 involves the case of single objects where there is no inter-object occlusion, but some objects have self-occlusion. The set of segmented images in Figure 7.18 involves multiple non-overlapped and overlapped objects. In the second set, the problems of false and missed regions are reduced using the successive split and merge method. The merge process is controlled primarily by the angle parameter between the surface normals of two adjacent regions. Using a large value for this angle yields a false merging of two adjacent regions that have a small angle between their surface normals.

Also, the boundaries of the objects in the images are refined and come close to the boundaries of the ideal (ground truth) segmented images in Figures 7.19 and 7.20.

Improving the boundaries is important in the next stages, vertex extraction and occlusion detection.

Computing the total reconstruction error for each segmented image according to equation (4.41) tests the reliability of the segmentation process. . The objective is to minimize this error, which is introduced as the residuals of the image that represent how well the data points are defined for the image.. The experiments produce a total reconstruction error for the initial segmented Perceptron range image of a value of 3.2 (cm). After the segmentation refinement stage, the total reconstruction error per image improves to 0.9 (cm).

Moreover, an objective comparison between the automatically computed segmentation system developed in this work and the ground truth results. The segmentation metric error in (2.10) is used to compare the correspondence regions for the results of the automatically computed segmentation system with the manually (ground truth) segmented range images. The segmentation metric error ranges from zero (if both segmentations are identical) to one (if a completely wrong correspondence is established where all corresponding regions are disjoint). This evaluation provided good results for the segmented images, with a figure of merit per image equaling 2.2%. Moreover, the segmentation results (region-based) of Hoover [43] are also compared with manually (ground truth) segmented range images using (2.10) and the figure of merit per image was 2.8%. This indicates that the accuracy of the results of the new segmentation approach (hybrid-based) is better than the results of Hoover's region-based approach.

Furthermore, the system takes a processing time of 145.5 (sec) per image for the initial segmentation stage, while this processing time is increased to 495.9 (sec) for the initial and refined segmentation. The images that have multiple overlapped objects take more processing time than those have single or multiple non-overlapped objects. All processing was done on a Sun UltraSPARC 1 workstation running the Solaris operating system. The codes of edge detection and segmentation were written in C and compiled using maximum optimization (-O4) with the gnu C (gcc) compiler.

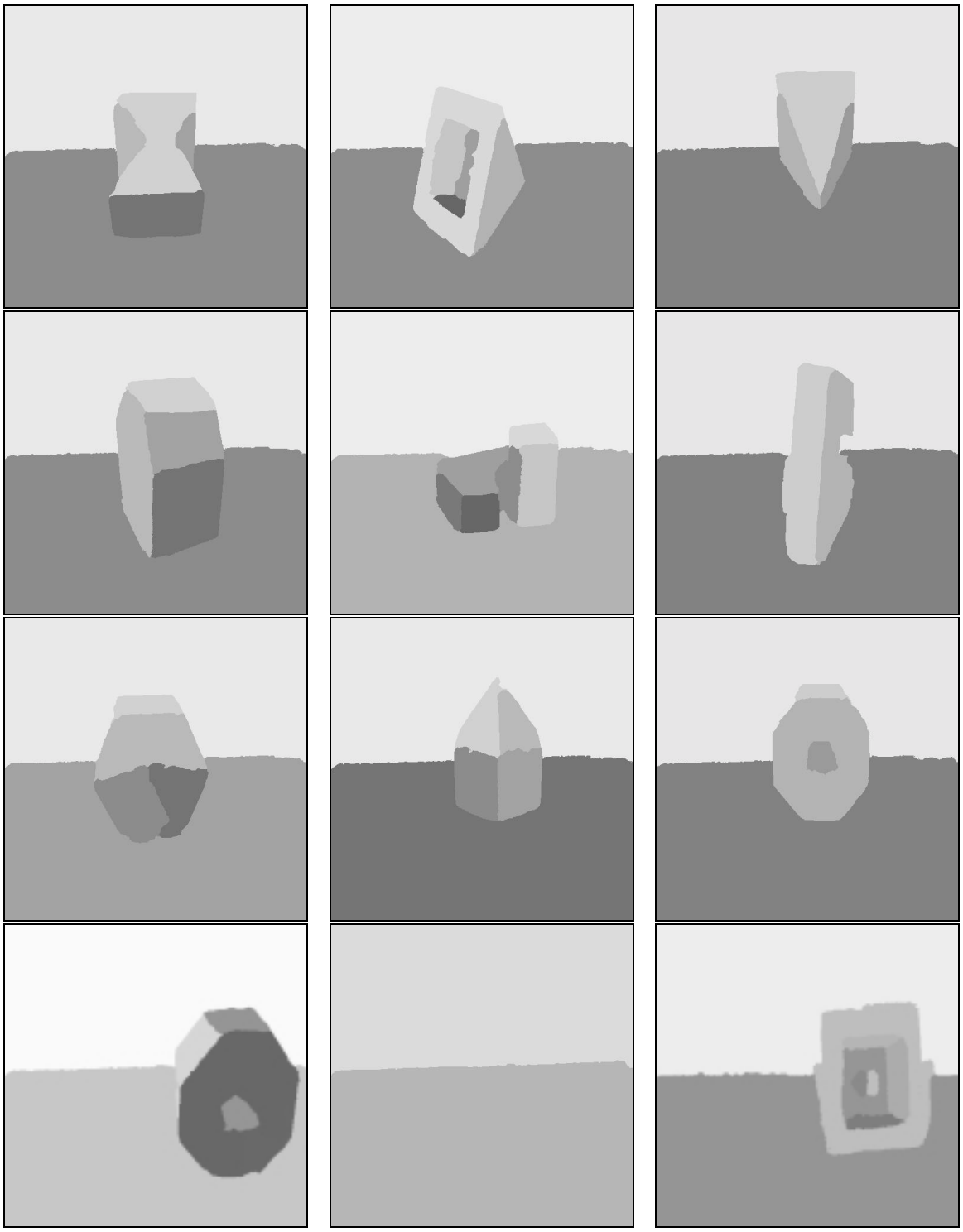

Figure 7.17 Results obtained by applying the segmentation approach to the Perceptron real range images of Figure 7.1. Most regions in the ranges are detected except those have size less than minimum allowable size to detect a region.

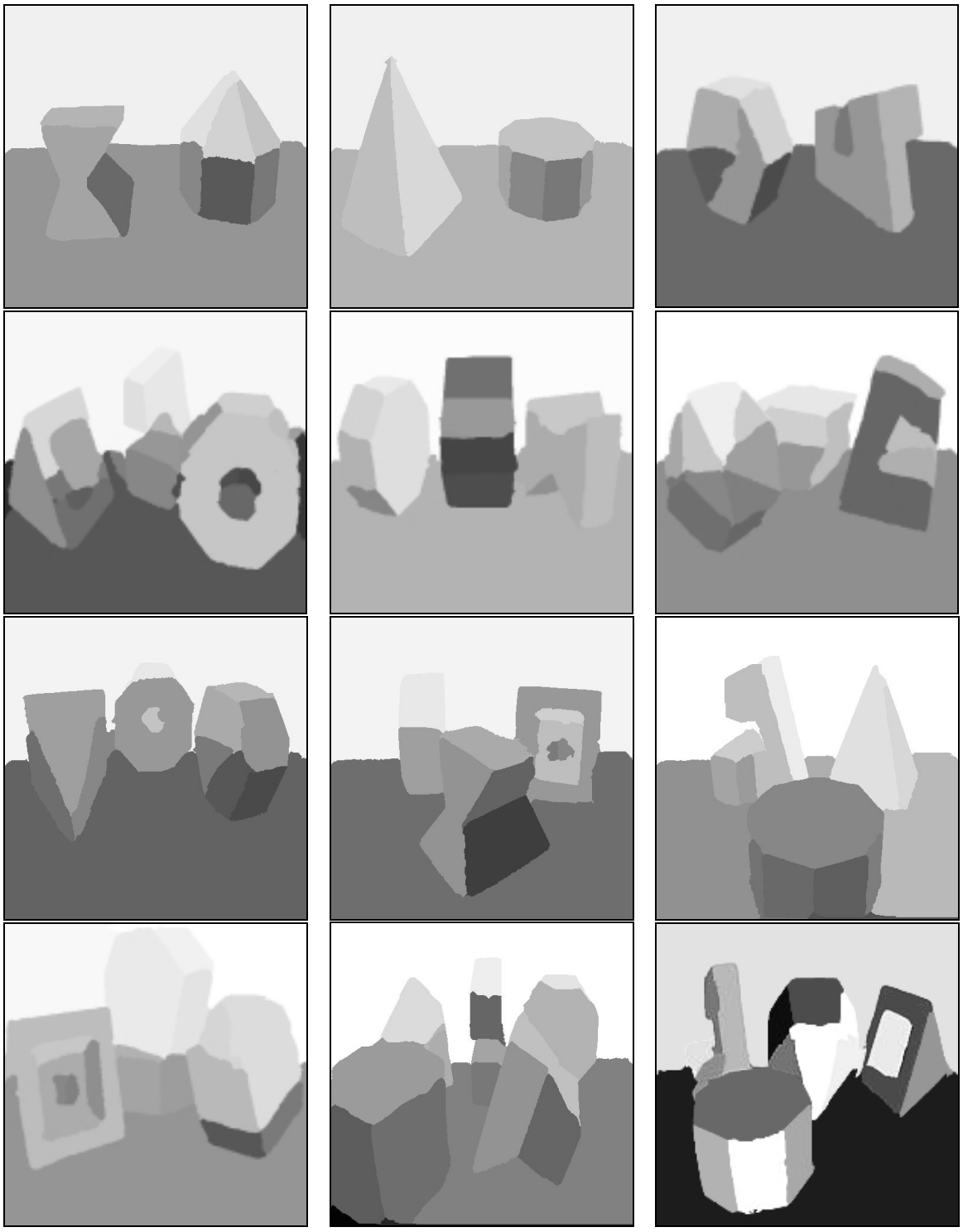

Figure 7.18 Results obtained by applying the segmentation technique on the real range image of Figure 7.2. Very few regions are merged with their adjacent region due to the angles between these surface normals are very small. The extracted overlapped objects are still considered as one objects so, occlusion detection approach will isolate these objects.

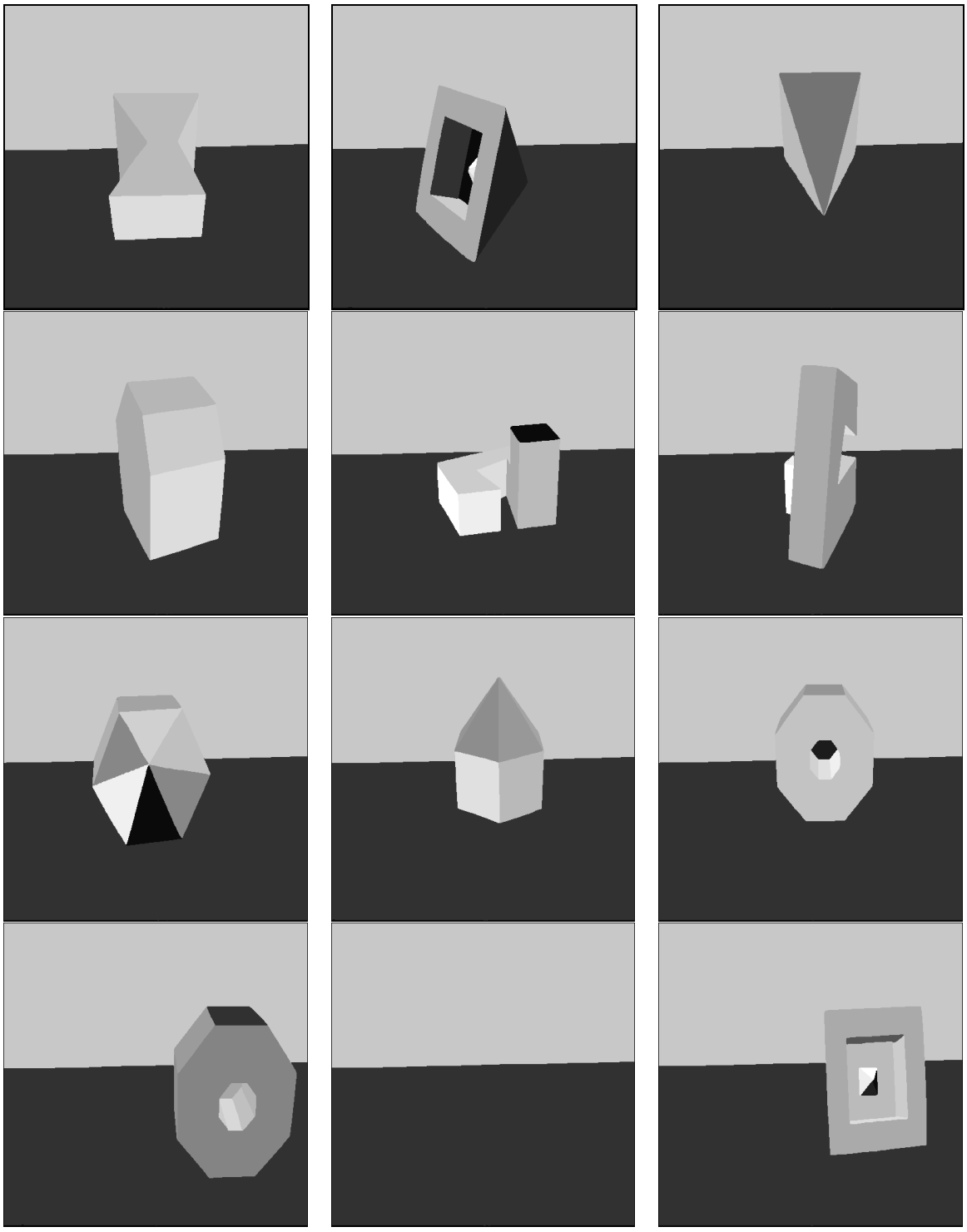

Figure 7.19 The ground truth segmentation for the real range images in Figure 7.1. These images were manually segmented and used for the purpose of the quantitative comparison with the proposed segmentation approach using the figure of merit criteria.

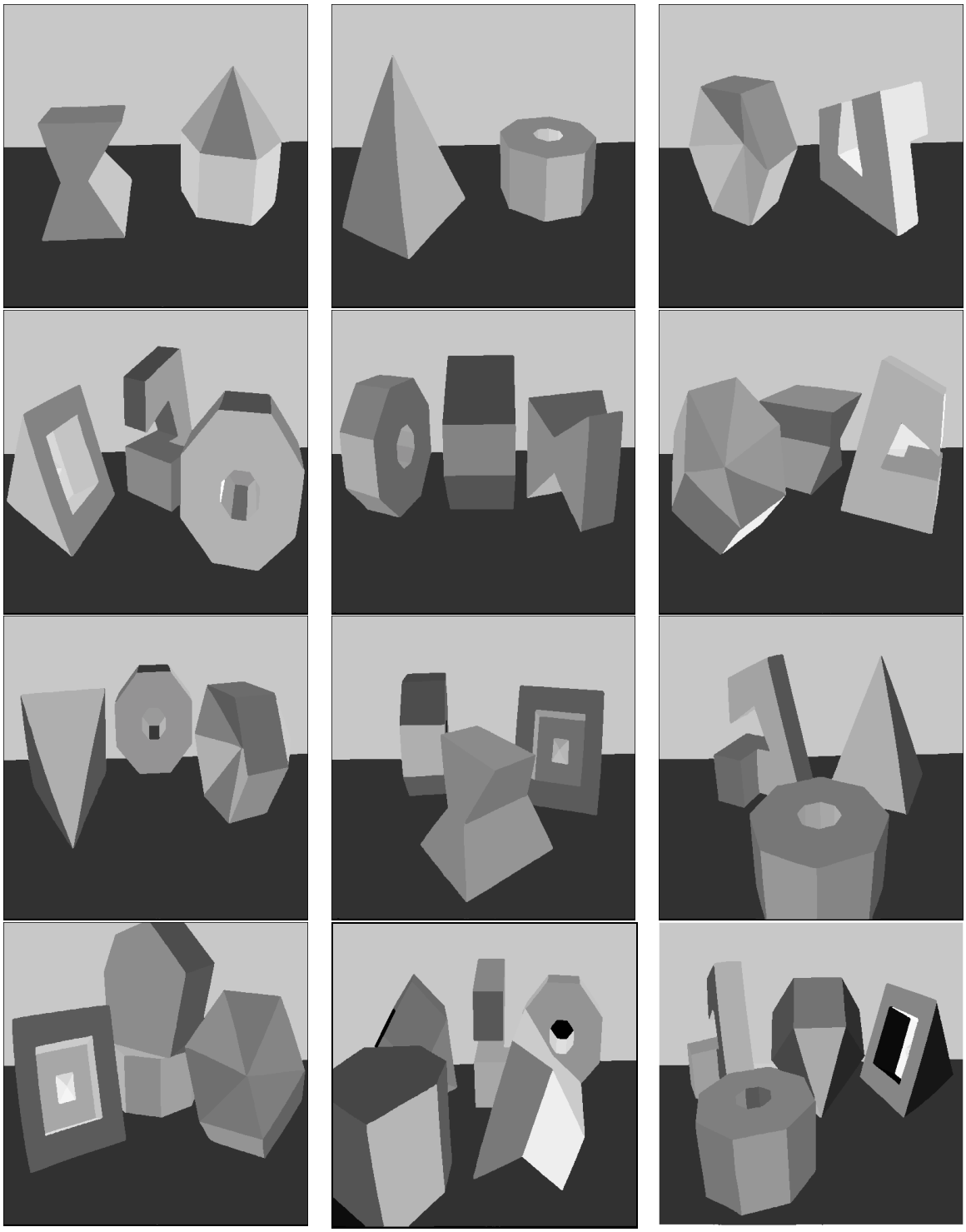

Figure 7.20 The ground truth segmentation for the real range images in Figure 7.2. These images were manually segmented and used for the purpose of the quantitative comparison with the proposed segmentation approach using the figure of merit criteria.

7.4 Examples For 3D-object Extraction and Representation

The proposed approach for extracting objects has been applied to several images. Although occlusion is present in most of the images, a few cases exhibit no occlusion. For all images, a simple background removal step removed the floor and a distant wall from consideration.

This section presents several examples of 3D-object extraction and representation. The goal of the extraction process is model description and representation. Some of the presented examples have single and multiple isolated objects; others have multiple overlapped objects. Occlusion detection is considered in these examples. The sequence of the examples indicates the occlusion complexity of the objects in the images.

Example #1

This example introduces the process of extracting and representing a single 3D object from a single range image. This case is relatively easy because of the lack of occlusion for visible surfaces of the object. Figure 7.20(a) represents a range image that has a single polyhedral. Figure 7.20(b) shows the smoothed histogram of the depth values for the object using Huber regression method. The intensity image is shown in Figure 7.20(c). Figure 7.20(d) shows the extracted 3D object in form of segmented image. Working from the segmented image, the system constructs the polyhedron representation illustrated in Figure 7.20(e). Figure 7.20(f) describes the region adjacency graph of the polyhedral. The model description of the entire range image is represented as

$$D = \{O_1\}$$
$$O_1 = \{S_1, V_1, G_1\}$$
$$S_1 = \{s_{1\text{-}1}, s_{1\text{-}2}, s_{1\text{-}3}, s_{1\text{-}4}\}$$
$$V_1 = \{v_{1\text{-}1}, v_{1\text{-}2}, v_{1\text{-}3}, v_{1\text{-}4}, v_{1\text{-}5}, v_{1\text{-}6}, v_{1\text{-}7}, v_{1\text{-}8}, v_{1\text{-}9}, v_{1\text{-}10}\}$$
$$G_1 = \{S_1, A_1\}$$
$$A_1 = \{a_{1-1}, a_{1-2}, a_{1-3}, a_{1-4}, a_{1-5}\}$$

The details of this description are shown in Tables 7.3-6. The line and surface parameters for this polyhedron are shown in Tables 7.3 and 7.4 respectively. The initial estimates of the 3D vertex locations in Cartesian coordinates extracted using the algorithm in Section 4.4 are presented in Table 7.5. In addition, a refinement process for the initial estimates of the 3D vertex locations is performed using the global optimization procedure introduced in Section 6.6.2. This refinement process is shown also in Table 7.5.

The significance of the optimization procedure is illustrated for the vertex $v_{12,}$ which has been moved the most of all vertices after optimization, where the initial estimate of the 3D coordinates was lying on the background of the image. The Euclidean distance between the initial estimate of v_{12} and the refined version is large (67.7 cm).

As expected, the initial estimates of vertices lying around the jump edges are quite inaccurate, for example, the vertex v_{12} has large distances (10.99 and 35.8) with the associated faces s_{11} and s_{12} as shown in Table 7.6. The 3D distances in cm between each initial and refined vertex with the associated faces of the object in Figure 7.22 before and after optimization are shown in Table 7.6. Because the vertices v_{13} and v_{110} are considered as the intersection of the planes of three faces, the distance between these vertices and their associated faces should be very small, as shown in Table 7.6.

The estimated errors are computed before and after optimization using both conventional mean and robust median estimators. The values using the mean estimator are 5.333 and 0.754, respectively. The values using the median estimator are 2.6 and 0.45, respectively. These values indicate the optimization improvement in the initial estimate of the 3D vertex locations and object representation. The optimization process is repeated 266 times, and the value of the objective function is equal to 5.77 at the final iteration. In the tables, the term “before optimization” indicates that these parameters are computed before optimization, as well as before the system starts to detect the occlusion.

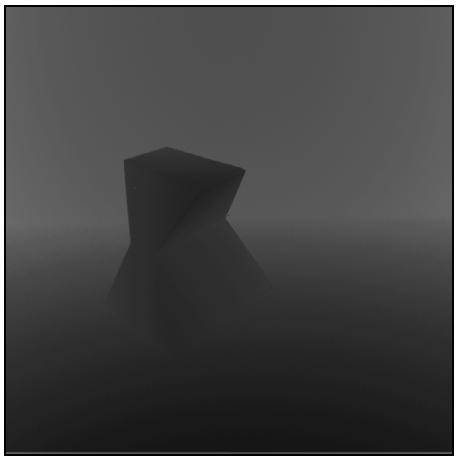

(a)

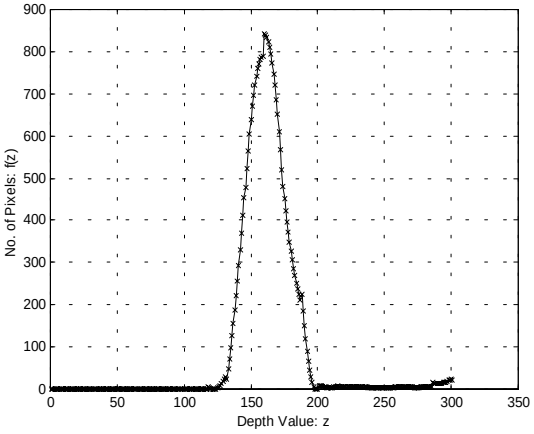

(b)

(c)

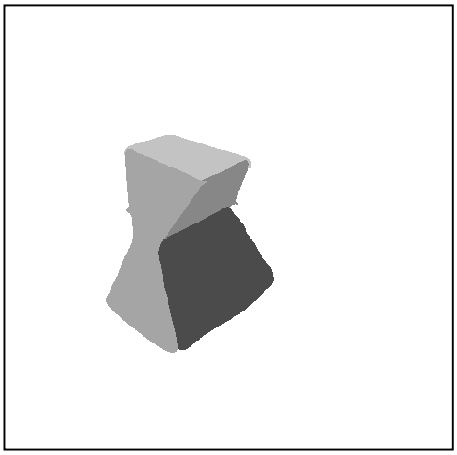

(d)

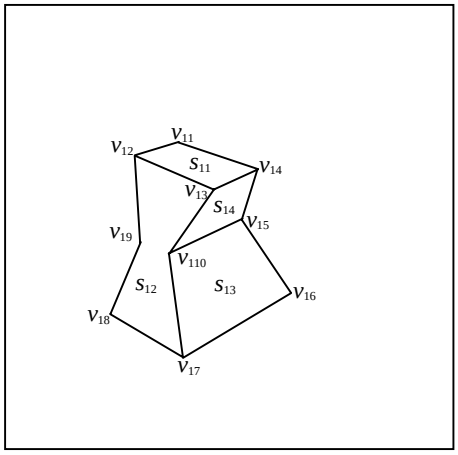

(e)

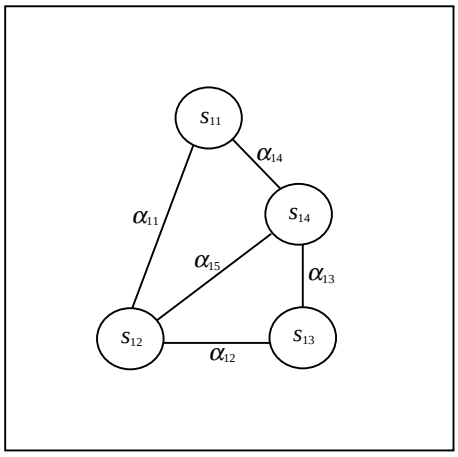

(f)

Figure 7.21 Example model construction of single polyhedral object from the range image, of size 512×512, obtained using a Perceptron range scanner. (a) Range image. (b) The smoothed histogram of the object. (c) Intensity image. (d) Segmented image. (e) The constructed model. (f) The region adjacency graph (RAG) of the object.

Table 7.3 The line parameters in 2D of the model of Figure 7.21(e).

S_1	Line	ρ	θ
s_{11}	v_{11} v_{12}	-210.600662	-16.927513
	v_{12} v_{13}	-205.511191	21.921779
	v_{13} v_{14}	-256.177460	-23.498566
	v_{14} v_{11}	275.325398	18.225075
s_{12}	v_{12} v_{19}	-46.405361	85.648922
	v_{19} v_{18}	-331.087482	-66.412969
	v_{18} v_{17}	115.634981	36.027373
	v_{17} v_{110}	383.518228	81.104143
	v_{110} v_{13}	234.880789	-56.496563
	v_{13} v_{12}	-205.511191	21.921779
s_{13}	v_{15} v_{110}	246.137894	-26.565051
	v_{110} v_{17}	383.518228	81.104143
	v_{17} v_{16}	-432.956234	-35.238225
	v_{16} v_{15}	367.858516	56.136309
s_{14}	v_{14} v_{13}	-256.177460	-23.498566
	v_{13} v_{110}	234.880789	-56.496563
	v_{110} v_{15}	246.137894	-26.565051
	v_{15} v_{14}	-205.850878	-72.216112

Table 7.4 The vertex sequence and surface parameters of the model of Figure 7.21(e).

S_1	Vertex sequence	a	b	c	d
s_{11}	$(v_{11}, v_{12}, v_{13}, v_{14})$	0.06	-0.98	0.19	-39.22
s_{12}	$(v_{12}, v_{19}, v_{18}, v_{17}, v_{110}, v_{13})$	-0.73	-0.09	0.67	-177.54
s_{13}	$(v_{15}, v_{110}, v_{17}, v_{16})$	0.44	-0.56	0.69	-240.25
s_{14}	$(v_{14}, v_{13}, v_{110}, v_{15})$	0.54	0.84	0.11	-41.70

Table 7.5 The initial estimate and optimized vertex locations of the model of Figure 7.21(e). The optimization procedure required 266 evaluations of the optimization criterion. The objective function value at the final iteration is 5.779.

	Before Optimization			After Optimization		
V_1	x_i	y_i	z_i	$\hat{x}_i$	$\hat{y}_i$	$\hat{z}_i$
v_{11}	44.4	40.49	348.2	35.5	33.8	342.3
v_{12}	82.3	37.7	388.4	62.3	27.1	324.6
v_{13}	17.0	15.7	282.8	11.23	12.22	281.3
v_{14}	-6.9	24.9	308.1	-12.0	21.3	311.4
v_{15}	2.7	4.9	342.4	-4.3	1.3	347.5
v_{16}	-27.7	-27.4	339.2	-35.5	-32.6	340.7
v_{17}	33.2	-51.7	290.7	30.7	-52.9	290.7
v_{18}	86.9	-35.8	336.7	82.4	-39.2	337.0
v_{19}	62.7	-5.4	318.8	53.4	-11.2	314.7
v_{110}	45.1	-10.2	306.8	43.7	-15.3	305.5

Table 7.6 The 3D distance in cm between each vertex and associated faces of the object in Figure 7.21. The estimated errors are computed before and after optimization using conventional mean and robust median estimators. The values using the mean estimator are 5.333 and 0.754, respectively. The values using the median estimator are 2.6 and 0.45, respectively.

	Before Optimization				After Optimization			
V_1-S_1	s_{11}	s_{12}	s_{13}	s_{14}	s_{11}	s_{12}	s_{13}	s_{14}
v_{11}	4.807				0.4607			
v_{12}	10.997	35.805			0.1810	0.0131		
v_{13}	2.863	2.814		6.221	0.0001	0.0002		0.0001
v_{14}	3.3391			8.292	1.1358			3.5810
v_{15}			0.4241	5.655			2.973	0.443
v_{16}			0.381				0.613	
v_{17}		2.146	1.828			0.4988	1.265	
v_{18}		1.752				1.5510		
v_{19}		2.413				0.6981		
v_{110}		0.183	0.768	5.307		0.0001	0.0002	0.0001

Example #2

Another example presents two isolated objects in the range image of Figure 7.22(a). The object on the left contains a self-occlusion case in which the face s_{12} is partially occluded by the faces s_{15} and s_{16}. The object on the right also involves self-occlusion at the vertex v_{27}. The object on the left will be considered in more detail.

Figure 7.22(b) presents the intensity images. Figure 7.22(c) contains the segmentation results. The system reconstructs two polyhedral objects as shown in Figure 7.22(d). Table 7.7 shows the vertex sequences and the computed plane parameters of the left object. The vertex sequence is useful in both the reconstruction process and the representation of the polyhedral objects.

Because of the self-occlusion, the system disassociates vertex v_{17} from the occluded face and substitutes the interior vertex v'_{17}, as described in Section 6.2. The optimization process then begins refining the whole set of initial estimates of vertices along with v'_{17}. Before occlusion detection, the 3D distance between the vertex v_{17} and the associated occluded face s_{12} is equal to 5.7; after occlusion detection, the 3D distance between the interior vertex v'_{17} and the face s_{12} has been improved to 0.1.

In this example, many initial estimates of vertices lying around jump edges are quite inaccurate, as shown in Table 7.8. The vertex v_{14} has large distances (6.0 and 86.0) with the associated faces s_{11} and s_{12}. In another case, the vertex v_{113} has large distances (122.0 and 38.0) with the associated faces s_{12} and s_{13}. The face s_{15} could be associated with the vertex v_{113} in case of the existence of a false corner for s_{15} close to v_{113}. This problem is not an occlusion case, but the system can handle it. The 3D distances between each initial and refined vertex and the associated faces of the object in Figure 7.22 before and after optimization are shown in Table 7.8.

The estimated errors are computed before and after optimization using the same estimators as in example #1. The values of the estimated errors using the mean estimator are 16.4 and 1.35, respectively, while the values of the estimated errors using the median

estimator are 6.4 and 1.2, respectively. These values indicate that the optimization procedure improved the initial estimate of the 3D vertex locations for the left object in the image, which yields progress in object representation.

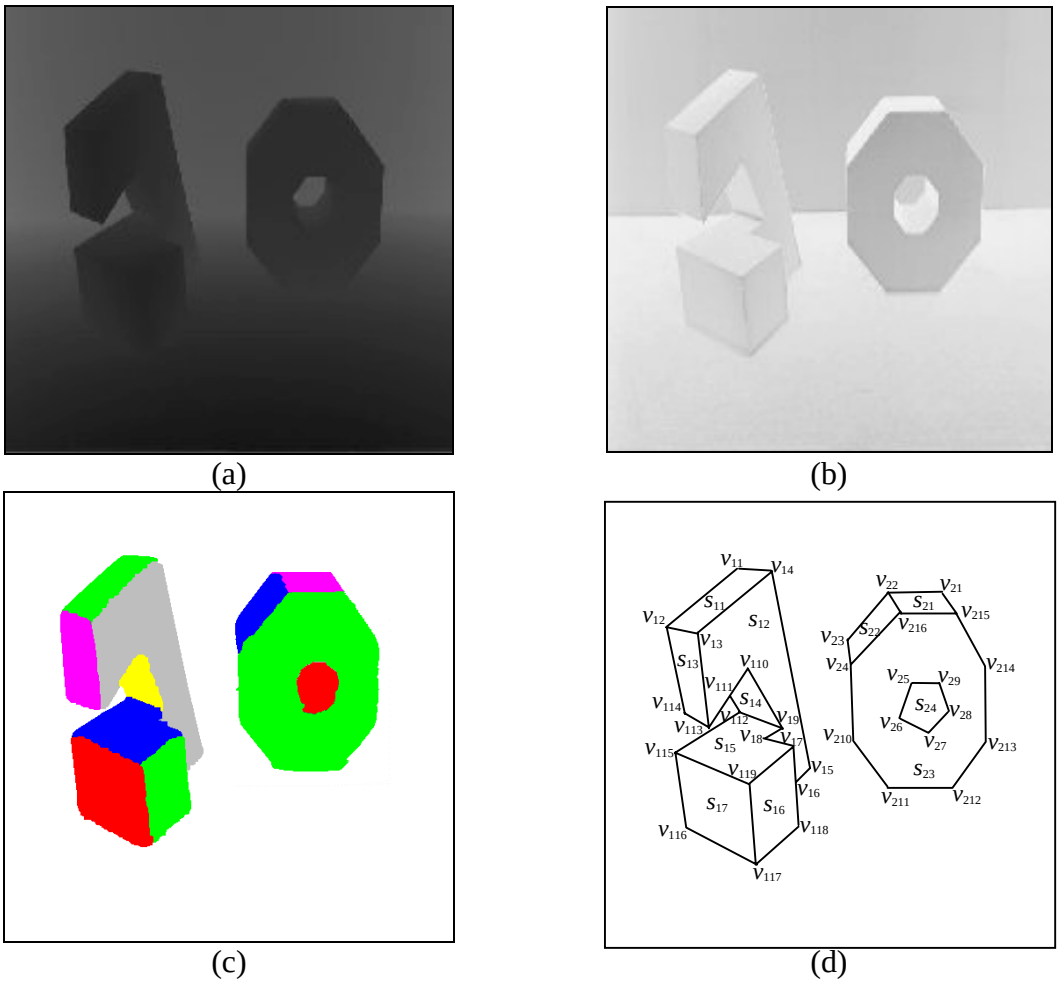

Figure 7.22 Example with self-occlusion. (a) Range image. (b) Intensity image. (c) Results of image segmentation. (d) The extracted objects. Without special consideration of partially occluded faces in the object at the left, the constructed model would contain many inaccuracies.

Table 7.7. The vertex sequences and surface parameters for the left object of Figure 7.22(d). The symbols *a-d* represent computed parameters of the planes fit through the respective object faces.

S_1	Vertex sequence	*a*	*b*	*c*	*d*
s_{11}	$(v_{11}, v_{12}, v_{13}, v_{14})$	-0.343	-0.842	0.414	-56.85
s_{12}	$(v_{14}, v_{13}, v_{113}, v_{110}, v_{19}, v_{18}, v'_{17}, v_{16}, v_{15})$	0.800	0.182	0.570	-218.0
s_{13}	$(v_{12}, v_{114}, v_{113}, v_{13})$	-0.826	0.302	0.474	-73.31
s_{14}	$(v_{110}, v_{111}, v_{112}, v_{19})$	-0.606	0.697	0.380	-99.69
s_{15}	$(v_{112}, v_{115}, v_{119}, v_{17}, v_{18}, v_{19})$	-0.049	-0.949	0.310	-104.6
s_{16}	$(v_{17}, v_{119}, v_{117}, v_{118})$	0.810	0.144	0.567	-189.6
s_{17}	$(v_{115}, v_{116}, v_{117}, v_{119})$	-0.577	0.302	0.758	-175.9

Table 7.8 The 3D distance in cm between each vertex and associated faces of the object in Figure 7.22. The estimated errors are computed before and after optimization using conventional mean and robust median estimators. The values using the mean estimator are 16.45 and 1.35, respectively. The values using the median estimator are 6.4 and 1.2, respectively.

	Before Optimization							After Optimization						
v-*s*	s_{11}	s_{12}	s_{13}	s_{14}	s_{15}	s_{16}	s_{17}	s_{11}	s_{12}	s_{13}	s_{14}	s_{15}	s_{16}	s_{17}
v_{11}	4.3							0.5						
v_{12}	14.		20.					1.9		2.4				
v_{13}	2.5	11.	1.5					0.0	0.0	0.0				
v_{14}	16.	86.						1.7	3.9					
v_{15}		7.8							2.3					
v_{16}		23.							2.7					
v_{17}		5.7			9.1	33.						2.2	1.4	
v_{18}		3.5			3.8				1.2			0.0		
v_{19}		4.8		4.9	3.8				0.0		0.0	0.0		
v_{110}		5.9		1.3					0.1		0.2			
v_{111}				16.							1.7			
v_{112}				12.	8.1						3.0	3.2		
v_{113}		122	38.						1.7	2.9				
v_{114}			8.6							1.3				
v_{115}					27.		50.					1.9		2.3
v_{116}							5.7							0.4
v_{117}						6.7	1.3						1.6	0.0
v_{118}				4.0							0.5			
v_{119}					1.0	6.1	0.9					0.0	0.0	0.0
v'_{17}		2.1							0.1					

Example #3

This example involves a complex case of multiple occlusions and introduces the capability of the system to extract, isolate, and represent these objects. Figure 7.23(a) illustrates the range image and Figure 7.23(b) presents the smoothed histogram of the object part of the range image. The segmented image is shown in Figure 7.23(c), and Figure 7.23(d) shows the jump edges that exist in this image along with the roof edges.

The system constructs the polyhedron representation illustrated in Figure 7.23(e). Applying the proposed geometric rules at the vertices of polyhedra, the system determines that occlusion exists at vertices *A*, *B*, and *C*. The objects O_1, O_2, and O_3 are isolated as shown in Figure 7.23(f).

Table 7.9 illustrates all pairs of adjacent faces that are associated with the vertices of the 3D object in Figure 7.23. The multiple evidence-based approach for detecting occlusion is used as described in Chapter 6. The measures of belief (*MB*1, *MB*2, *MB*3, *MB*4, and *MB5*) produced by the five rules, along with the certainty factors (*CF*1, *CF*2, and *CF*3) computed using three combining methods as described in Section 6.3.5, are applied for each pair of adjacent faces. Occlusion is detected for 10 of the 36 pairs of adjacent faces, as highlighted in the shaded rows in Table 7.9.

This occlusion detection is performed at each vertex; thus, a pair of adjacent of faces may be repeated at different vertices, as shown in Table 7.9. Pairs that are repeated in Table 7.9 are listed only once in Table7.10, and the certainty factor associated with those pairs (for example, rows 1 and 7; rows 30, 33, and 34) are the combination of the corresponding repeated certainty factors in Table 7.9. The false, missed, and correct detection rates of occlusion are computed for each combining method. The correct rates for all combining methods are 100%, while the false rate of the first combining method is 100% at threshold value 30%.

Table 7.11(a) illustrates the region adjacency graph (RAG) table for the image in Figure 7.23. Table 7.11(b) presents the augmented RAG after detecting the occlusion between adjacent faces associated to each vertex. Table 7.11(c) depicts the grouping of faces

according to the adjacency relationship, where this image has three objects as shown in Figure 7.23(f). Figures 7.23 and 7.24 show the histogram for some cases of no occlusion and occlusion between two adjacent faces of Figure 7.23. The original histogram is smoothed using the robust regression method described in Section 5.3.2. The single mode histograms show the case of adjacent pairs that have no occlusion, while the cases of bimodal histogram represents the occlusion between these pairs.

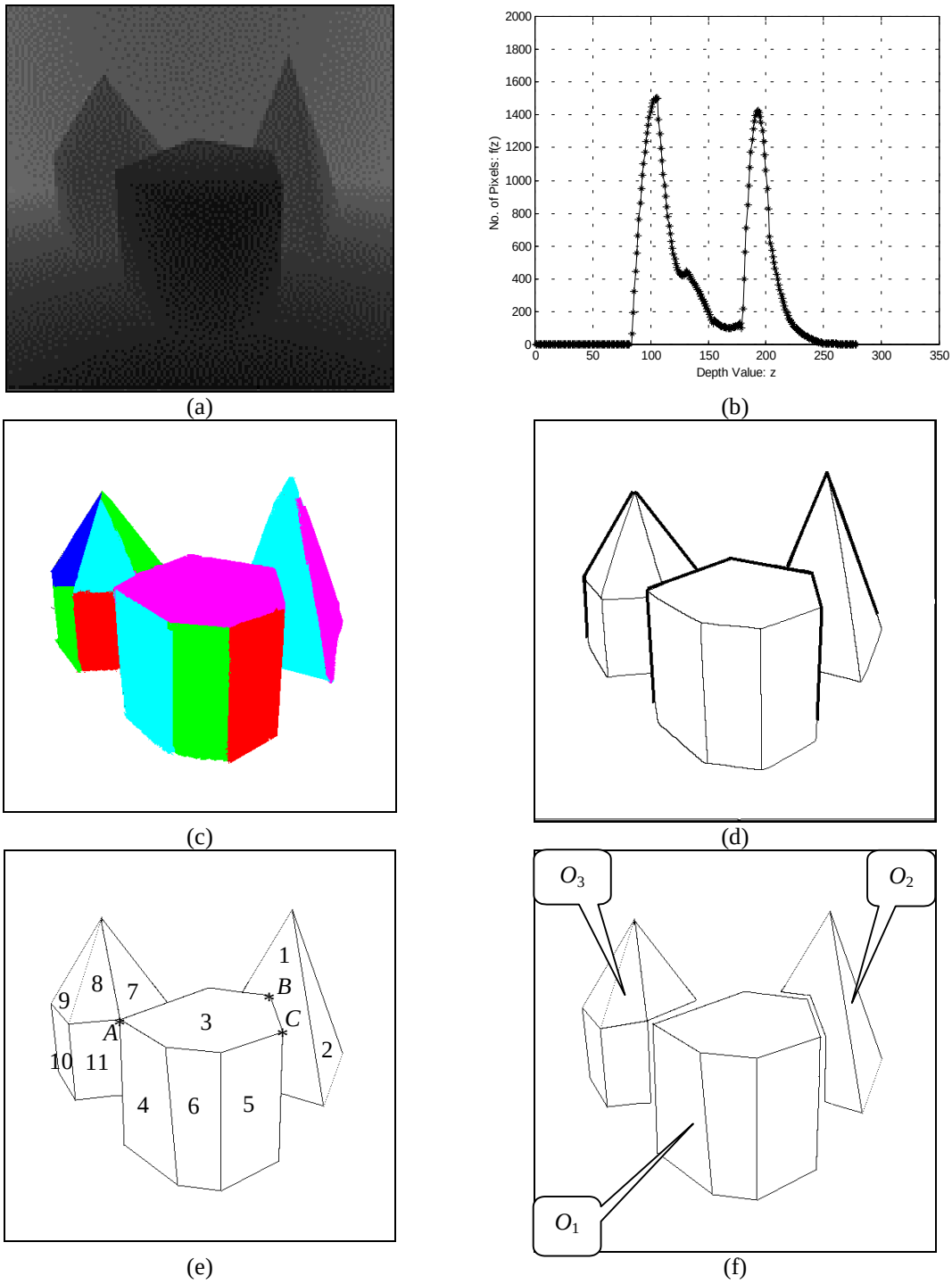

Figure 7.23 Inter-object occlusion example. (a) Range image. (b) Histogram of the object part in the range image. (c) Results of image segmentation. (d) Results of jump edges (thicker lines) in addition to roof edges (thicker lines). (e) The extracted objects, without special consideration of partially occluded faces. (f) Three extracted and isolated objects, with consideration of partially occluded faces.

Table 7.9 Detection of occlusion for the object in Figure 7.23(e) This table depicts each pair of adjacent faces and the values of the measure of belief for each rule applied to this pair. *CF*1 is the certainty factor computed using MYCIN-style inference. *CF*2 is the certainty factor computed using the voting criteria three of six. *CF*3 is computed using the weighted average method. The shaded rows represent the pairs of faces that should have occlusion.

#	s_i	s_j	*MB*1	*MB*2	*MB*3	*MB*4	*MB*5	*CF*1	*CF*2	*CF*3
1	10	11	0.319	0.105	0.146	0.010	0.365	0.693	0.170	0.208
2	8	9	0.321	0.218	0.183	0.010	0.275	0.720	0.273	0.211
3	8	10	0.327	0.285	0.220	0.010	0.347	0.766	0.256	0.247
4	8	11	0.105	0.057	0.079	0.010	0.035	0.340	0.099	0.057
5	9	10	0.317	0.119	0.085	0.010	0.084	0.561	0.170	0.133
6	9	11	0.207	0.242	0.238	0.010	0.293	0.689	0.238	0.200
7	10	11	0.319	0.137	0.168	0.010	0.365	0.712	0.199	0.217
8	3	4	0.195	0.049	0.060	0.010	0.078	0.350	0.068	0.086
9	3	7	0.814	0.519	0.179	0.942	0.573	0.998	0.998	0.637
10	3	8	0.772	0.501	0.548	0.784	0.632	0.996	0.996	0.661
11	3	11	0.798	0.532	0.446	0.817	0.648	0.997	0.997	0.668
12	4	7	0.872	0.624	0.404	0.010	0.782	0.994	0.994	0.571
13	4	8	0.851	0.560	0.530	0.991	0.838	1.000	1.000	0.778
14	4	11	0.856	0.569	0.619	0.010	0.857	0.997	0.997	0.607
15	7	8	0.217	0.124	0.175	0.010	0.194	0.580	0.193	0.149
16	7	11	0.050	0.215	0.234	0.010	0.192	0.551	0.075	0.132
17	8	11	0.105	0.119	0.147	0.010	0.035	0.429	0.145	0.078
18	9	10	0.317	0.756	0.175	0.010	0.084	0.890	0.203	0.254
19	7	8	0.217	0.054	0.179	0.010	0.194	0.549	0.129	0.138
20	8	9	0.321	0.056	0.241	0.010	0.275	0.686	0.160	0.192
21	3	5	0.169	0.084	0.127	0.010	0.319	0.557	0.103	0.154
22	3	6	0.114	0.033	0.049	0.010	0.429	0.544	0.052	0.147
23	5	6	0.095	0.061	0.126	0.010	0.201	0.469	0.159	0.103
24	5	6	0.095	0.084	0.138	0.010	0.201	0.489	0.179	0.109
25	4	6	0.148	0.156	0.123	0.010	0.478	0.735	0.260	0.199
26	4	6	0.148	0.045	0.401	0.010	0.478	0.795	0.194	0.221
27	3	4	0.195	0.066	0.039	0.010	0.078	0.347	0.058	0.086
28	3	6	0.114	0.055	0.019	0.010	0.429	0.540	0.039	0.147
29	4	6	0.148	0.712	0.870	0.010	0.478	0.987	0.315	0.404
30	1	3	0.834	0.739	0.763	0.711	0.777	0.999	0.999	0.769
31	1	5	0.974	0.135	0.799	0.999	0.987	1.000	1.000	0.813
32	3	5	0.169	0.412	0.738	0.010	0.319	0.915	0.186	0.299
33	1	3	0.834	0.034	0.097	0.711	0.777	0.991	0.991	0.552
34	1	3	0.834	0.078	0.509	0.711	0.777	0.995	0.995	0.619
35	1	2	0.469	0.081	0.146	0.010	0.250	0.696	0.105	0.213
36	1	2	0.469	0.692	0.699	0.010	0.250	0.964	0.269	0.398

Table 7.10 The decision table after combining the certainty factor of any two adjacent faces repeated in Table 7.9. Also, thresholding the certainty factor *CF*1, *CF*2, and *CF*3 with 30% to find the occlusion in the adjacent pairs. The false, missed, and correct rate of detection of occlusion are computed for each combining method after combining the measures of belief at 30% thresholding. The letter 'O' means that one of the two surfaces occludes the other. Also, O(*A*) indicates that there is an occlusion at the vertex *A* in Figure 7.23(e).

#	s_i	s_j	*MB*1	*MB*2	*MB*3	*MB*4	*MB*5	*CF*1	30%	*CF*2	30%	*CF*3	30%
1	10	11	0.319	0.105	0.146	0.010	0.365	0.693	O	0.170		0.208	
2	8	9	0.321	0.218	0.183	0.010	0.275	0.720	O	0.273		0.211	
3	8	10	0.327	0.285	0.220	0.010	0.347	0.766	O	0.256		0.247	
4	8	11	0.105	0.057	0.079	0.010	0.035	0.340	O	0.099		0.057	
5	9	10	0.317	0.119	0.085	0.010	0.084	0.561	O	0.170		0.133	
6	9	11	0.207	0.242	0.238	0.010	0.293	0.689	O	0.238		0.200	
7	3	4	0.195	0.049	0.060	0.010	0.078	0.350	O	0.068		0.086	
8	3	7	0.814	0.519	0.179	0.942	0.573	0.998	O(*A*)	0.998	O(*A*)	0.637	O(*A*)
9	3	8	0.772	0.501	0.548	0.784	0.632	0.996	O(*A*)	0.996	O(*A*)	0.661	O(*A*)
10	3	11	0.798	0.532	0.446	0.817	0.648	0.997	O(*A*)	0.997	O(*A*)	0.668	O(*A*)
11	4	7	0.872	0.624	0.404	0.010	0.782	0.994	O(*A*)	0.994	O(*A*)	0.571	O(*A*)
12	4	8	0.851	0.560	0.530	0.991	0.838	1.000	O(*A*)	1.000	O(*A*)	0.778	O(*A*)
13	4	11	0.856	0.569	0.619	0.010	0.857	0.997	O(*A*)	0.997	O(*A*)	0.607	O(*A*)
14	7	8	0.217	0.124	0.175	0.010	0.194	0.580	O	0.193		0.149	
15	7	11	0.050	0.215	0.234	0.010	0.192	0.551	O	0.075		0.132	
16	3	5	0.169	0.084	0.127	0.010	0.319	0.557	O	0.103		0.154	
17	3	6	0.114	0.033	0.049	0.010	0.429	0.544	O	0.052		0.147	
18	5	6	0.095	0.061	0.126	0.010	0.201	0.469	O	0.159		0.103	
19	4	6	0.148	0.156	0.123	0.010	0.478	0.735	O	0.260		0.199	
20	1	3	0.834	0.739	0.763	0.711	0.777	0.999	O(*B*)	0.999	O(*B*)	0.769	O(*B*)
21	1	5	0.974	0.135	0.799	0.999	0.987	1.000	O(*C*)	1.000	O(*C*)	0.813	O(*C*)
22	1	2	0.469	0.081	0.146	0.010	0.250	0.696	O	0.105		0.213	

False Rate of Occlusion	1.00	0.00	0.00
Missed Rate of Occlusion	0.00	0.00	0.00
Correct Rate of Occlusion	1.00	1.00	1.00

Table 7.11 The region adjacency graph table (RAG) for the segmented image of Figure 7.23(c), after occlusion detection, with grouping of faces. (a) The RAG after final segmentation. (b) The augmented RAG after detecting the occlusion between the adjacent faces. (c) Grouping the faces that belong to the same object according to the adjacent relationship between the faces on Table 7.11(b).

Face#	Adjacent faces						
1	2	3	5				
2	1						
3	1	4	5	6	7	8	11
4	3	6	7	8	11		
5	1	3	6				
6	3	4	5				
7	3	4	8	11			
8	3	4	7	11			
9	8	10	11				
10	8	9	11				
11	3	4	7	8	9	10	

(a)

Face#	Adjacent faces						
1	2						
2	1						
3		4	5	6			
4	3	6					
5		3	6				
6	3	4	5				
7			8	11			
8			7	11			
9	8	10	11				
10	8	9	11				
11			7	8	9	10	

(b)

Objects	Faces belonging to objects				
O_1	3	4	5	6	
O_2	1	2			
O_3	7	8	9	10	11

(c)

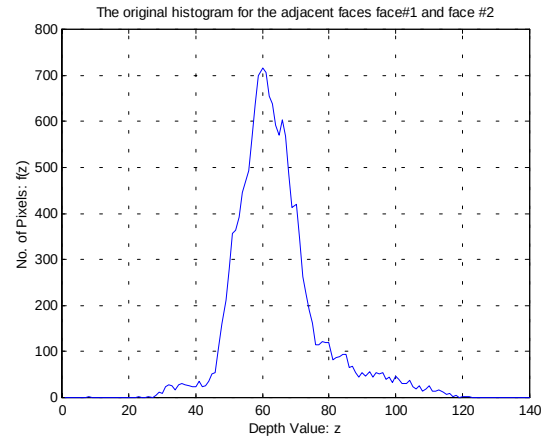

(a)

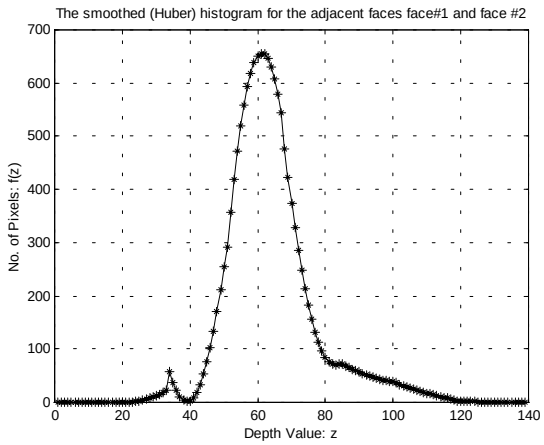

(b)

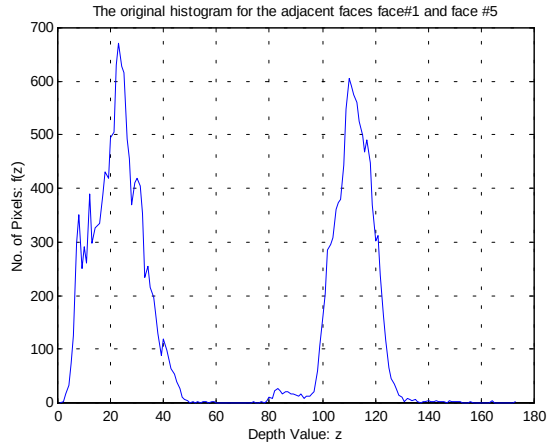

(c)

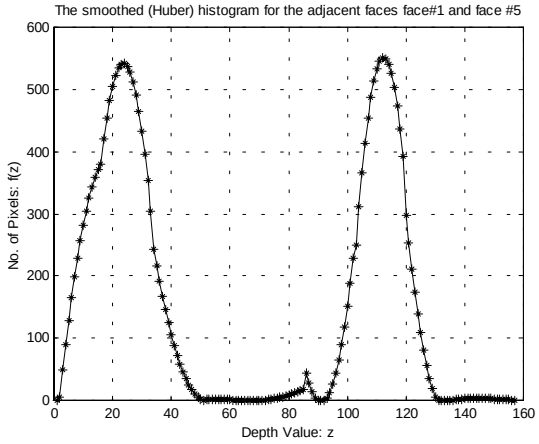

(d)

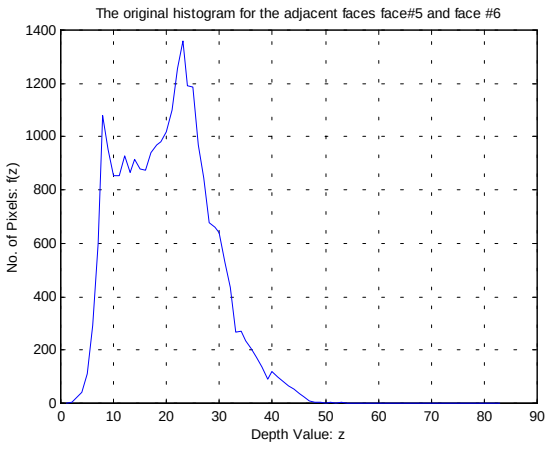

(e)

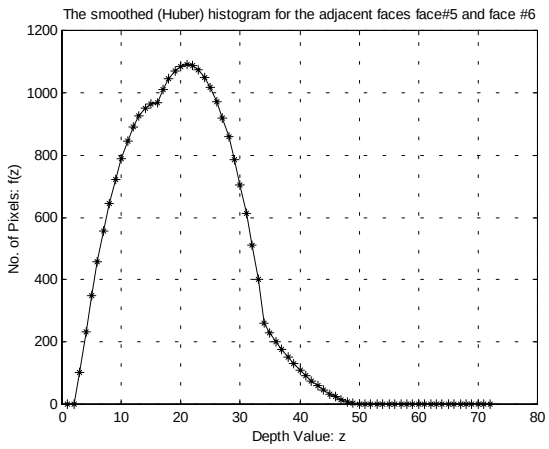

(f)

Figure 7.24 The original histogram for adjacent faces of the image in Figure 7.23(e) and its smoothed version using Huber linear regression. (a) Histogram of faces #1 and #2. (c) Histogram of faces #1 and #5. (e) Histogram of faces #5 and #6.

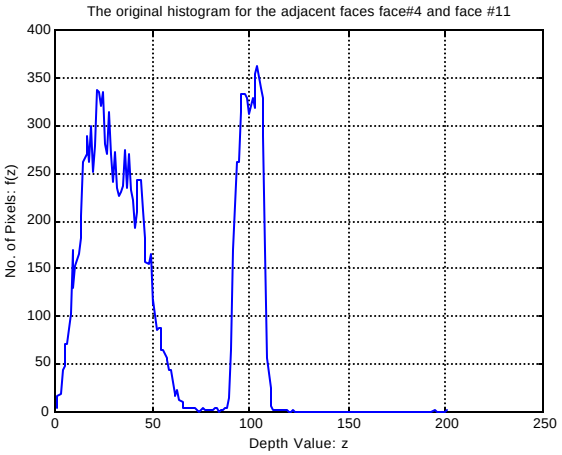

(a)

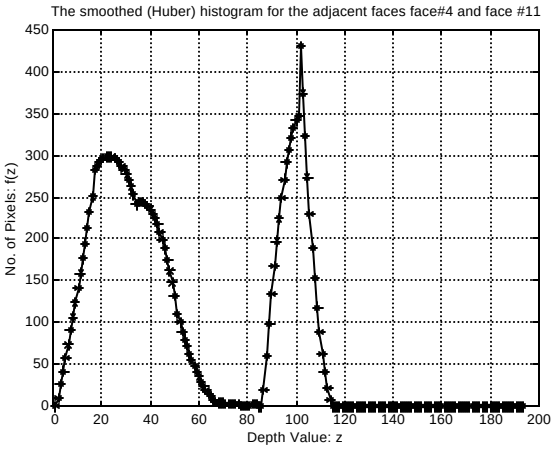

(b)

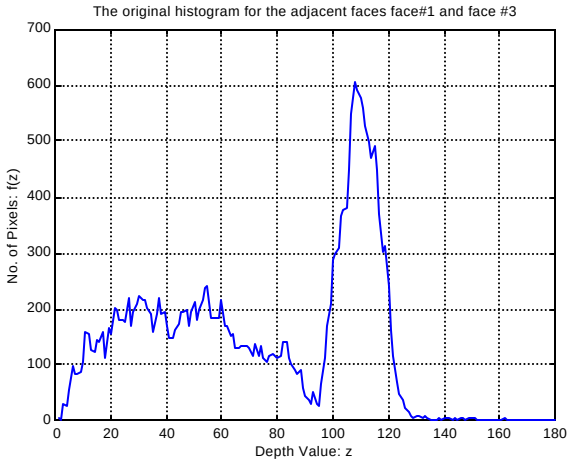

(c)

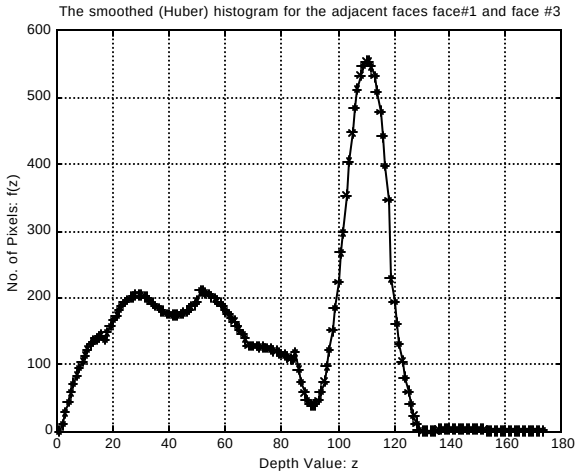

(d)

Figure 7.25 The original histogram for adjacent faces of the image in Figure 7.23(e) and its smoothed version using Huber linear regression. (a) Histogram of faces #4 and #11. (c) Histogram of faces #1 and #3.

Example #4

This example is more complex than the previous one and also represents a case of multiple inter-object occlusions. The range image is illustrated in Figure 7.26(a). Figure 7.26(b) presents the smoothed histogram of the object part of the range image. The edges are obtained via the gradient direction using adaptive Gaussian method as shown in Figure 7.26(c). The segmented image is shown in Figure 7.26(d). The system constructs the boundary representation of the polyhedrons illustrated in Figure 7.26(e). Applying the proposed geometric rules, objects O_1, O_2, O_3, O_4, and O_5 are isolated after detecting the occlusion as shown in Figure 7.26(f).

The measures of belief and certainty factors (*MB*1, *MB*2, *MB*3, *MB*4, *MB*5, *CF*1, *CF*2, and *CF*3) for all pairs of adjacent faces associated with the vertices of the 3D object in Figure 7.26 are illustrated in Table 7.12. Twenty-nine of 78 pairs of adjacent faces have occlusion, shown in the highlighted rows in Table 7.12.

The occlusion detection is performed at each vertex; therefore, a pair of adjacent faces may be repeated at different vertices as shown in different rows in Table 7.12. Table 7.13 introduces each pair of adjacent faces once, associated with its certainty factor, which is the combination of the repeated certainty factors appearing in Table 7.12. The false, missed, and correct rate of detection of occlusion are computed for each combining method after combining the measures of belief. The correct rates for all combining methods are (100%, 72%, and 89%), while the false rates are (84%, 4%, and 1%), respectively. The certainty factors for the adjacent pairs of faces that are very close in the real world have small values {(6,11) = 0.49, (4,10) = 0.32, (20,24) = 0.19}, which indicates that the measures of beliefs of the rules are also small.

Table 7.14(a) illustrates the region adjacency graph (RAG) table of the object part for the image in Figure 7.26. Table 7.14(b) presents the augmented RAG after detecting the occlusion between adjacent faces associated with each vertex. Table 7.14(c) depicts the grouping of faces according to the adjacency relationship, where this image has the five objects as shown in Figure 7.26(f).

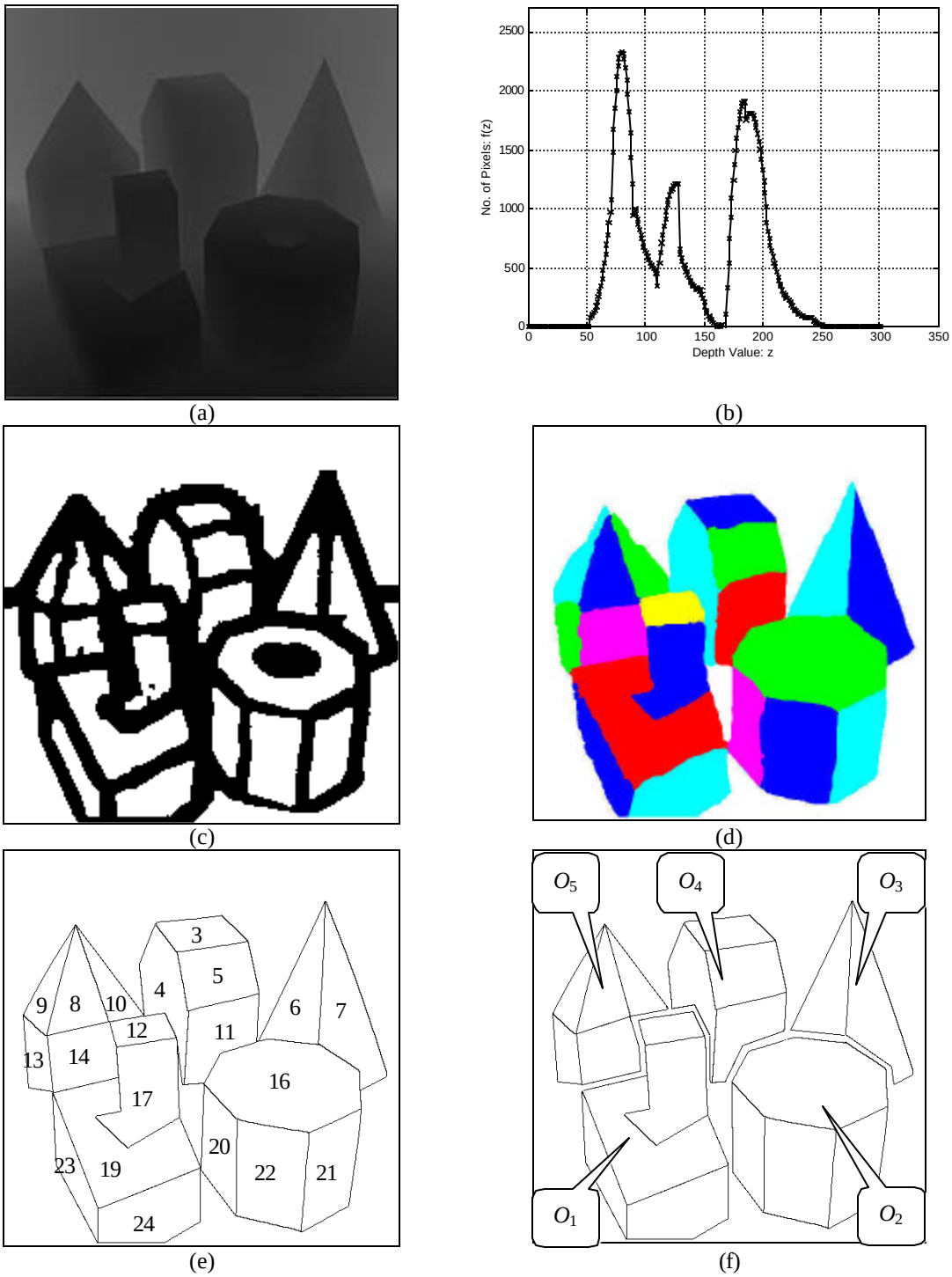

Figure 7.26 Inter-object occlusion example. (a) Range image. (b) Histogram of the object part in the range image. (c) Results of image segmentation. (d) Results of jump edges (thicker lines) in addition to roof edges. (e) The extracted objects, without special consideration of partially occluded faces. (f) Three extracted and isolated objects, with consideration of partially occluded faces.

Table 7.12 Detection of occlusion for the object in Figure 7.26(e) This table depicts each pair of adjacent faces and the values of the measure of belief for each rule applied to this pair. *CF*1 is the certainty factor computed using MYCIN-style inference. *CF*2 is the certainty factor computed with the voting criteria three of six. *CF*3 is computed using the weighted average method. The shaded rows represent the pairs of faces that should have occlusion.

#	s_i	s_i	*MB*1	*MB*2	*MB*3	*MB*4	*MB*5	*CF*1	*CF*2	*CF*3
1	3	5	0.180	0.111	0.229	0.010	0.278	0.598	0.120	0.164
2	3	4	0.239	0.068	0.050	0.644	0.046	0.771	0.094	0.220
3	3	5	0.180	0.069	0.097	0.010	0.278	0.507	0.078	0.139
4	4	5	0.239	0.097	0.106	0.010	0.174	0.498	0.106	0.135
5	3	4	0.239	0.050	0.061	0.644	0.046	0.769	0.094	0.218
6	4	5	0.239	0.167	0.186	0.010	0.174	0.578	0.176	0.157
7	4	11	0.244	0.055	0.087	0.010	0.140	0.445	0.064	0.118
8	5	11	0.103	0.035	0.094	0.010	0.069	0.277	0.045	0.063
9	4	11	0.244	0.073	0.108	0.010	0.140	0.467	0.082	0.124
10	4	12	0.918	0.592	0.304	0.991	0.473	1.000	1.000	0.687
11	4	17	0.964	0.565	0.557	0.991	0.811	1.000	1.000	0.810
12	12	17	0.171	0.050	0.061	0.010	0.148	0.377	0.060	0.098
13	4	12	0.918	0.614	0.295	0.991	0.473	1.000	1.000	0.689
14	4	10	0.000	0.645	0.403	0.642	0.075	0.930	0.075	0.313
15	4	12	0.918	0.629	0.346	0.991	0.473	1.000	1.000	0.699
16	10	12	0.699	0.594	0.406	0.976	0.660	0.999	0.999	0.689
17	5	11	0.103	0.039	0.084	0.010	0.069	0.272	0.049	0.062
18	6	7	0.140	0.040	0.090	0.010	0.019	0.270	0.028	0.060
19	6	7	0.140	0.069	0.098	0.010	0.019	0.298	0.028	0.066
20	6	16	0.818	0.334	0.275	0.991	0.874	1.000	1.000	0.712
21	7	16	0.863	0.365	0.208	0.991	0.912	1.000	1.000	0.729
22	6	11	0.979	0.377	0.383	0.010	0.546	0.996	0.384	0.494
23	6	16	0.818	0.757	0.658	0.991	0.874	1.000	1.000	0.835
24	11	16	0.819	0.549	0.373	0.991	0.758	1.000	1.000	0.734
25	7	16	0.863	0.806	0.623	0.991	0.912	1.000	1.000	0.859
26	7	16	0.863	0.712	0.511	0.991	0.912	1.000	1.000	0.829
27	8	9	0.273	0.079	0.276	0.010	0.272	0.651	0.088	0.187
28	8	10	0.254	0.135	0.256	0.010	0.223	0.630	0.144	0.177
29	9	10	0.992	0.136	0.172	0.010	0.040	0.995	0.049	0.304
30	8	10	0.254	0.043	0.087	0.010	0.223	0.498	0.053	0.138
31	8	12	0.255	0.473	0.517	0.010	0.736	0.950	0.263	0.395
32	8	14	0.087	0.043	0.079	0.010	0.065	0.255	0.052	0.057
33	10	12	0.699	0.450	0.206	0.976	0.660	0.999	0.999	0.638
34	10	14	0.835	0.072	0.072	0.477	0.301	0.948	0.139	0.400
35	12	14	0.892	0.370	0.314	0.010	0.807	0.991	0.321	0.526
36	8	9	0.273	0.071	0.120	0.010	0.272	0.572	0.080	0.165
37	8	13	0.244	0.070	0.056	0.010	0.364	0.582	0.065	0.171
38	8	14	0.087	0.042	0.086	0.010	0.065	0.260	0.052	0.058
39	9	13	0.272	0.033	0.074	0.010	0.099	0.419	0.042	0.109
40	9	14	0.251	0.114	0.155	0.010	0.366	0.648	0.123	0.194
41	13	14	0.302	0.201	0.224	0.010	0.446	0.763	0.209	0.250
42	9	13	0.272	0.041	0.308	0.010	0.099	0.569	0.050	0.141
43	11	16	0.819	0.492	0.401	0.991	0.758	1.000	1.000	0.728
44	11	16	0.819	0.665	0.529	0.991	0.758	1.000	1.000	0.774
45	11	20	0.956	0.708	0.600	0.999	0.925	1.000	1.000	0.868
46	16	20	0.192	0.073	0.074	0.010	0.065	0.358	0.075	0.088
47	12	14	0.892	0.597	0.543	0.010	0.807	0.996	0.996	0.595
48	12	17	0.171	0.045	0.065	0.010	0.148	0.376	0.054	0.097
49	14	17	0.941	0.632	1.000	0.010	0.990	1.000	1.000	0.719
50	14	17	0.941	0.620	1.000	0.010	0.990	1.000	1.000	0.717

51	14	19	0.609	0.334	0.306	0.692	0.736	0.985	0.985	0.570
52	17	19	0.418	0.397	0.341	0.010	0.332	0.847	0.339	0.300
53	13	14	0.302	0.133	0.158	0.010	0.446	0.720	0.142	0.230
54	13	19	0.742	0.489	0.228	0.975	0.656	0.999	0.999	0.657
55	13	23	0.938	0.137	0.744	0.993	0.569	1.000	1.000	0.696
56	14	19	0.609	0.341	0.317	0.692	0.736	0.986	0.986	0.573
57	14	23	0.000	0.242	0.208	0.762	0.660	0.951	0.208	0.386
58	19	23	0.277	0.496	0.138	0.010	0.081	0.714	0.090	0.194
59	16	20	0.192	0.023	0.021	0.010	0.065	0.286	0.031	0.073
60	16	22	0.100	0.094	0.054	0.010	0.325	0.484	0.064	0.130
61	20	22	0.142	0.125	0.132	0.010	0.387	0.605	0.134	0.171
62	16	21	0.130	0.051	0.089	0.010	0.177	0.387	0.061	0.098
63	16	22	0.100	0.066	0.050	0.010	0.325	0.466	0.059	0.124
64	21	22	0.108	0.057	0.089	0.010	0.231	0.416	0.066	0.107
65	17	19	0.418	0.192	0.155	0.010	0.332	0.737	0.163	0.240
66	17	19	0.418	0.373	0.321	0.010	0.332	0.836	0.328	0.293
67	17	19	0.418	0.054	0.070	0.010	0.332	0.661	0.064	0.206
68	19	20	0.000	0.347	0.219	0.010	0.045	0.518	0.010	0.102
69	19	24	0.112	0.078	0.103	0.010	0.203	0.421	0.087	0.107
70	20	24	0.000	0.260	0.239	0.010	0.462	0.700	0.010	0.192
71	19	23	0.277	0.042	0.045	0.010	0.081	0.398	0.051	0.104
72	19	24	0.112	0.068	0.076	0.010	0.203	0.397	0.077	0.101
73	23	24	0.310	0.104	0.117	0.010	0.305	0.624	0.113	0.187
74	20	22	0.142	0.042	0.062	0.010	0.387	0.532	0.051	0.148
75	16	21	0.130	0.070	0.091	0.010	0.177	0.401	0.080	0.102
76	21	22	0.108	0.143	0.102	0.010	0.231	0.477	0.111	0.123
77	23	24	0.310	0.057	0.145	0.010	0.305	0.617	0.066	0.182
78	17	19	0.418	0.060	0.034	0.010	0.332	0.650	0.044	0.202

Table 7.13 The decision table after combining the certainty factor of any two adjacent faces repeated in Table 7.12. Also, thresholding the certainty factor *CF*1, *CF*2, and *CF*3 with 30% to find the occlusion in the adjacent pairs. The false, missed, and correct rate of detection of occlusion are computed for each combining method after combining the measures of belief at 30% thresholding. The letter 'O' means that one of the two surfaces occludes the other.

#	S_i	s_j	*MB*1	*MB*2	*MB*3	*MB*4	*MB*5	*CF*1	30%	*CF*2	30%	*CF*3	30%
1	3	5	0.180	0.111	0.229	0.010	0.278	0.598	O	0.120		0.164	
2	3	4	0.239	0.068	0.050	0.644	0.046	0.771	O	0.094		0.220	
3	4	5	0.239	0.097	0.106	0.010	0.174	0.498	O	0.106		0.135	
4	4	11	0.244	0.055	0.087	0.010	0.140	0.445	O	0.064		0.118	
5	5	11	0.103	0.035	0.094	0.010	0.069	0.277		0.045		0.063	
6	4	12	0.918	0.592	0.304	0.991	0.473	1.000	O	1.000	O	0.687	O
7	4	17	0.964	0.565	0.557	0.991	0.811	1.000	O	1.000	O	0.810	O
8	12	17	0.171	0.050	0.061	0.010	0.148	0.377	O	0.060		0.098	
9	4	10	0.000	0.645	0.403	0.642	0.075	0.930	O	0.075		0.313	O
10	10	12	0.699	0.594	0.406	0.976	0.660	0.999	O	0.999	O	0.689	O
11	6	7	0.140	0.040	0.090	0.010	0.019	0.270		0.028		0.060	
12	6	16	0.818	0.334	0.275	0.991	0.874	1.000	O	1.000	O	0.712	O
13	7	16	0.863	0.365	0.208	0.991	0.912	1.000	O	1.000	O	0.729	O
14	6	11	0.979	0.377	0.383	0.010	0.546	0.996	O	0.384		0.494	O
15	11	16	0.819	0.549	0.373	0.991	0.758	1.000	O	1.000	O	0.734	O
16	8	9	0.273	0.079	0.276	0.010	0.272	0.651	O	0.088		0.187	
17	8	10	0.254	0.135	0.256	0.010	0.223	0.630	O	0.144		0.177	
18	9	10	0.992	0.136	0.172	0.010	0.040	0.995	O	0.049		0.304	
19	8	12	0.255	0.473	0.517	0.010	0.736	0.950	O	0.263		0.395	O
20	8	14	0.087	0.043	0.079	0.010	0.065	0.255		0.052		0.057	
21	10	14	0.835	0.072	0.072	0.477	0.301	0.948	O	0.139		0.400	
22	12	14	0.892	0.370	0.314	0.010	0.807	0.991	O	0.321	O	0.526	O
23	8	13	0.244	0.070	0.056	0.010	0.364	0.582	O	0.065		0.171	
24	9	13	0.272	0.033	0.074	0.010	0.099	0.419	O	0.042		0.109	
25	9	14	0.251	0.114	0.155	0.010	0.366	0.648	O	0.123		0.194	
26	13	14	0.302	0.201	0.224	0.010	0.446	0.763	O	0.209		0.250	
27	11	20	0.956	0.708	0.600	0.999	0.925	1.000	O	1.000	O	0.868	O
28	16	20	0.192	0.073	0.074	0.010	0.065	0.358	O	0.075		0.088	
29	14	17	0.941	0.632	1.000	0.010	0.990	1.000	O	1.000	O	0.719	O
30	14	19	0.609	0.334	0.306	0.692	0.736	0.985	O	0.985	O	0.570	O
31	17	19	0.418	0.397	0.341	0.010	0.332	0.847	O	0.339		0.300	
32	13	19	0.742	0.489	0.228	0.975	0.656	0.999	O	0.999	O	0.657	O
33	13	23	0.938	0.137	0.744	0.993	0.569	1.000	O	1.000	O	0.696	O
34	14	23	0.000	0.242	0.208	0.762	0.660	0.951	O	0.208		0.386	O
35	19	23	0.277	0.496	0.138	0.010	0.081	0.714	O	0.090		0.194	
36	16	22	0.100	0.094	0.054	0.010	0.325	0.484	O	0.064		0.130	
37	20	22	0.142	0.125	0.132	0.010	0.387	0.605	O	0.134		0.171	
38	16	21	0.130	0.051	0.089	0.010	0.177	0.387	O	0.061		0.098	
39	21	22	0.108	0.057	0.089	0.010	0.231	0.416	O	0.066		0.107	
40	19	20	0.000	0.347	0.219	0.010	0.045	0.518	O	0.010		0.102	
41	19	24	0.112	0.078	0.103	0.010	0.203	0.421	O	0.087		0.107	
42	20	24	0.000	0.260	0.239	0.010	0.462	0.700	O	0.010		0.192	
43	23	24	0.310	0.104	0.117	0.010	0.305	0.624	O	0.113		0.187	

False Rate of Occlusion	0.84	0.04	0.01
Missed Rate of Occlusion	0.00	0.28	0.10
Correct Rate of Occlusion	1.00	0.72	0.89

Table 7.14 The region adjacency graph table (RAG) for the segmented image of Figure 7.26(c), after occlusion detection, and faces grouping. (a) The RAG after final segmentation. (b) The augmented RAG after detecting the occlusion between the adjacent faces. (c) Grouping the faces that belong to the same object according to the adjacent relationship between the faces on Table 7.14(b).

Face#	Adjacent faces							
3	5	4						
4	3	5	11	12	17	10		
5	3	4	11					
6	7	16	11					
7	6	16						
8	9	10	12	14	13			
9	8	10	13	14				
10	4	12	8	9	14			
11	4	5	6	16	20			
12	4	17	0	8	14			
13	8	9	14	19	23			
14	8	10	12	9	13	17	19	23
16	6	7	11	20	22	21		
17	4	12	14	19				
19	14	17	13	23	20	24		
20	11	16	22	19	24			
21	16	22						
22	16	20	21					
23	1 3	14	19	24				
24	19	20	23					

(a)

Face#	Adjacent faces						
3	5	4					
4	3	5	11				
5	3	4	11				
6	7						
7	6						
8	9	10		14			
9	8		13				
10			8				
11	4	5					
12		17					
13		9	14				
14	8				3		
16				20	22	21	
17		12		19			
19		17	13		20	24	
20		16	22		24		
21	16	22					
22	16	20	21				
23			19	24			
24	19		23				

(b)

Objects	Faces belonging to objects				
O_1	12	17	19	23	24
O_2	16	20	21	22	
O_3	6	7			
O_4	3	4	5	11	
O_5	8	9	10	13	14

(c)

7.5 Evaluation of the Results for the Occlusion Detection Multiple Evidence-based Approach

The performance evaluation of the results for the multiple evidence-based occlusion detection approach is very important in determining the capability and limitation of this algorithm. To evaluate this approach, the performance of the rules was tested in terms of false alarm and missed and correct detection rates of occlusion. The weights of the rules depend on the correct detection rate for each rule, assuming that the rule is applied individually to detect occlusion. These weights are used to measure the reliability of the rules. The performance of the combining methods, weighted average, voting, and certainty factor (MYCIN) for the measures of belief were also evaluated. While these methods provide good results in terms of correct detection rate, the certainty factor method produces high false alarm rate.

When a rule is applied individually a high correct detection rate is more important than a low false alarm rate. The false alarm rate can be solved using the combining method discussed in chapter 6.

Figures 7.27-32 and Table 7.15 show the false, missed, and correct detection rates of occlusion for the measure of beliefs (*MBs*), along with the combining methods at different levels of certainty confidence. The goodness of each rule is measured as the capability of this rule to individually detect an occlusion between pairs of adjacent faces with the low false alarm rate as shown in Figures 7.27, 7.28, and 7.29(a). The reliability of the combining methods for the measures of belief is considered an important issue in deciding occlusion as shown in Figures 7.29(b) and 7.30.

Figure 7.31 illustrates a comparison between the performance of the five rules in terms of correct detection rate of occlusion, along with low false rate; Rule #1 and Rule #5 are considered the best with respect to the other rules. The weighted average and voting methods provide good results in terms of correct detection rate of occlusion, as well as a lower false rate than the certainty factor (MYCIN) method, as shown in Figure 7.32.

Selecting the threshold value for the certainty factor (*CF*) produced by combining the measure of beliefs (*MBs*) should achieve the optimality of correct rate and false alarm detection. A small threshold value yields high correct and false alarm rates, and a large threshold value yields small correct and false alarm rates. The optimal threshold value used in this work was 30%, which yields the following results:

MBs and CFs	Correct detection rate	False alarm rate
MB1	0.86	0.25
MB2	0.82	0.08
MB3	0.75	0.08
MB4	0.52	0.05
MB5	0.93	0.35
CF1	1.00	0.91
CF2	0.88	0.04
CF3	0.96	0.05

The above results show that Rule #5 and #1 are considered the best of the five, even though they both have high false alarm rates. These high false alarm rates are solved when the voting (CF2) or the weighted average (CF3) combining methods is applied.

The weights were chosen in the weighted average scheme as the correct rates for the rules when each rule is used individually in occlusion detection. Hence, the weight values are 0.86, 0.82, 0.75, 0.52 and 0.93 for the five rules respectively.

Table 7.15 Performance evaluation for the multiple evidence-based system. These tables evaluate the false, missed, and correct detection rates of occlusion for the measures of belief *MBs* of the rules and the combining methods of these measures of beliefs *CFs* at different certainty levels. (a) False rate. (b) Missed rate. (c) Correct rate.

(a)

%	*MB*1	*MB*2	*MB*3	*MB*4	*MB*5	*CF*1	*CF*2	*CF*3
0	1.00	1.00	1.00	1.00	1.00	1.00	1.00	1.00
10	0.91	0.37	0.55	0.16	0.72	1.00	0.45	0.80
20	0.52	0.16	0.20	0.04	0.57	1.00	0.13	0.28
30	0.27	0.09	0.09	0.04	0.35	0.91	0.04	0.05
40	0.12	0.07	0.05	0.04	0.09	0.79	0.00	0.01
50	0.03	0.04	0.04	0.03	0.00	0.60	0.00	0.00
60	0.03	0.04	0.04	0.03	0.00	0.41	0.00	0.00
70	0.03	0.03	0.03	0.00	0.00	0.25	0.00	0.00
80	0.03	0.00	0.01	0.00	0.00	0.11	0.00	0.00
90	0.01	0.00	0.00	0.00	0.00	0.07	0.00	0.00

(b)

%	*MB*1	*MB*2	*MB*3	*MB*4	*MB*5	*CF*1	*CF*2	*CF*3
0	0.00	0.00	0.00	0.00	0.00	0.00	0.00	0.00
10	0.10	0.05	0.03	0.44	0.05	0.00	0.08	0.00
20	0.10	0.10	0.05	0.46	0.05	0.00	0.08	0.05
30	0.13	0.15	0.26	0.46	0.05	0.00	0.13	0.05
40	0.13	0.33	0.44	0.46	0.05	0.00	0.18	0.13
50	0.13	0.44	0.56	0.46	0.15	0.00	0.18	0.15
60	0.13	0.69	0.79	0.46	0.23	0.03	0.18	0.31
70	0.23	0.87	0.87	0.54	0.38	0.05	0.18	0.62
80	0.31	0.97	0.95	0.56	0.64	0.05	0.18	0.85
90	0.74	1.00	0.95	0.56	0.82	0.05	0.18	1.00

(c)

%	*MB*1	*MB*2	*MB*3	*MB*4	*MB*5	*CF*1	*CF*2	*CF*3
0	1.00	1.00	1.00	1.00	1.00	1.00	1.00	1.00
10	0.90	0.95	0.97	0.56	0.95	1.00	0.92	1.00
20	0.90	0.90	0.95	0.54	0.95	1.00	0.92	0.95
30	0.87	0.85	0.74	0.54	0.95	1.00	0.87	0.95
40	0.87	0.67	0.56	0.54	0.95	1.00	0.82	0.87
50	0.87	0.56	0.44	0.54	0.85	1.00	0.82	0.85
60	0.87	0.31	0.21	0.54	0.77	0.97	0.82	0.69
70	0.77	0.13	0.13	0.46	0.62	0.95	0.82	0.38
80	0.69	0.03	0.05	0.44	0.36	0.95	0.82	0.15
90	0.26	0.00	0.05	0.44	0.18	0.95	0.82	0.00

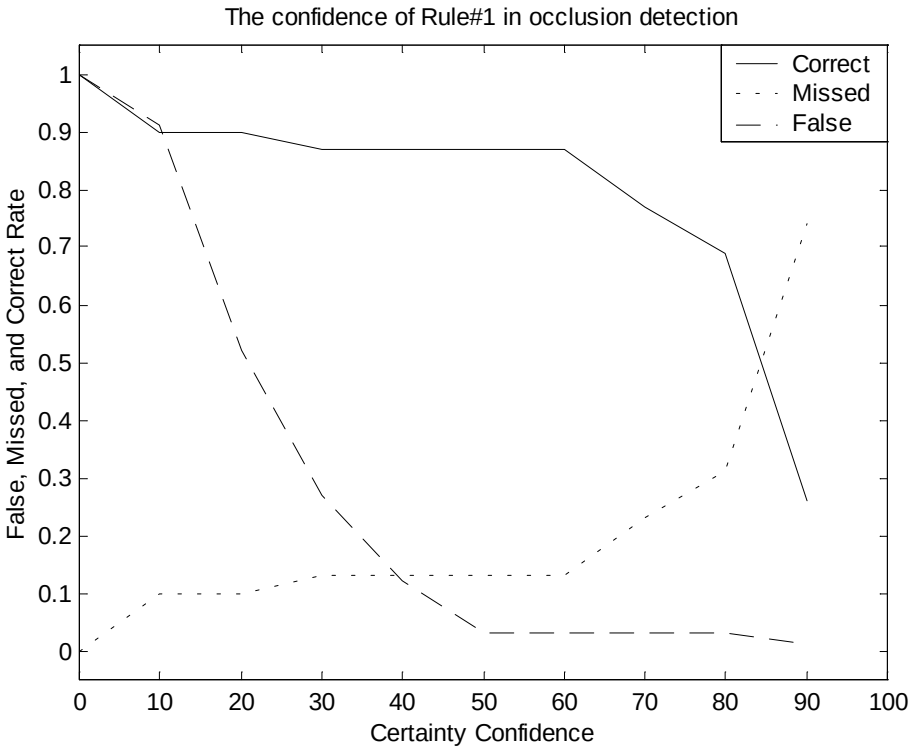

(a)

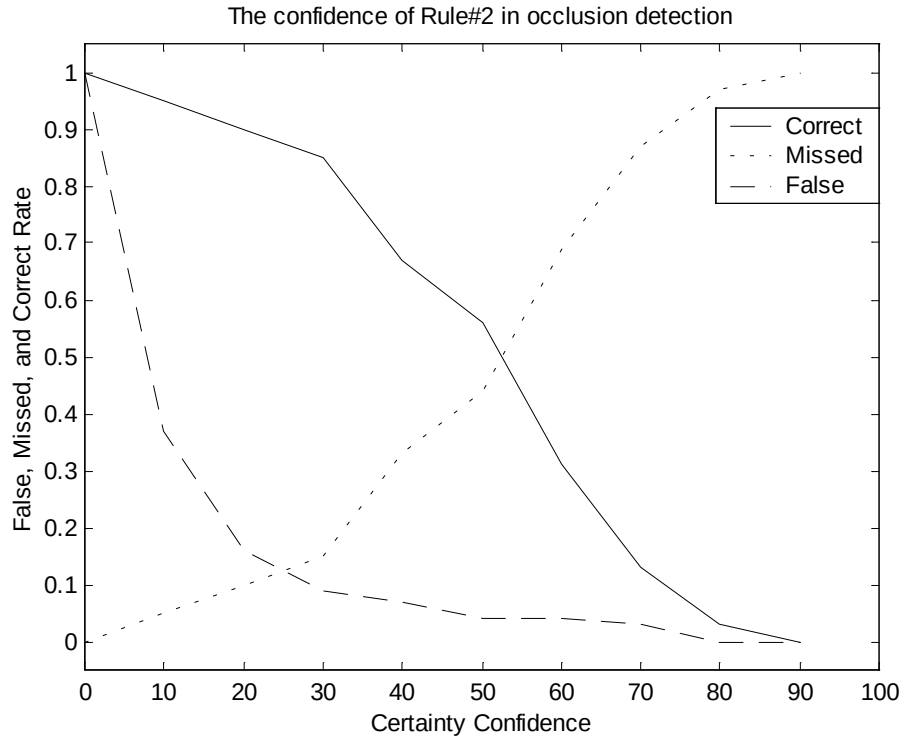

(b)

Figure 7.27 The certainty confidence for Rule #1 and Rule #2. This is computed through measure of false, missed, and correct detection of occlusion at different certainty. (a) Rule#1. (b) Rule#2.

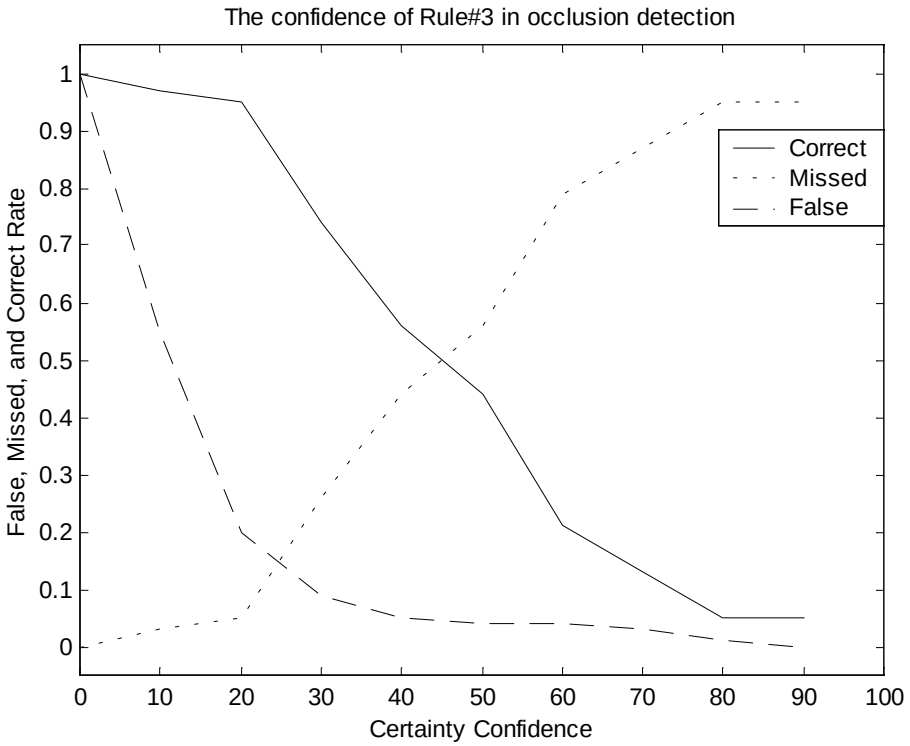

(a)

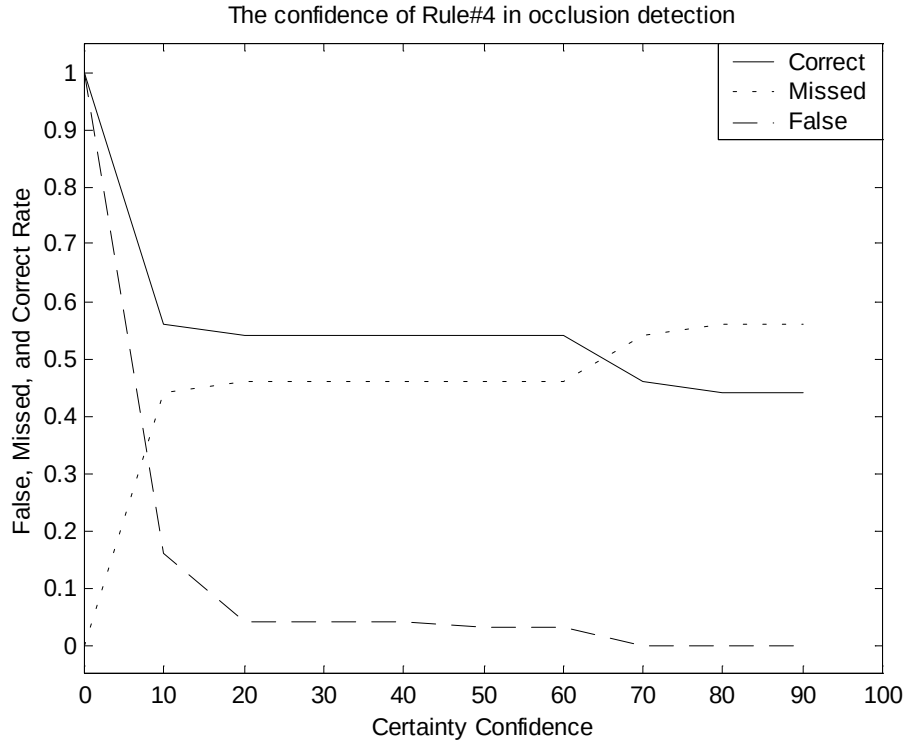

(b)

Figure 7.28 The certainty confidence for Rule #3 and Rule #4. This is computed through measure of false, missed, and correct detection of occlusion at different certainties. (a) Rule#3. (b) Rule#4.

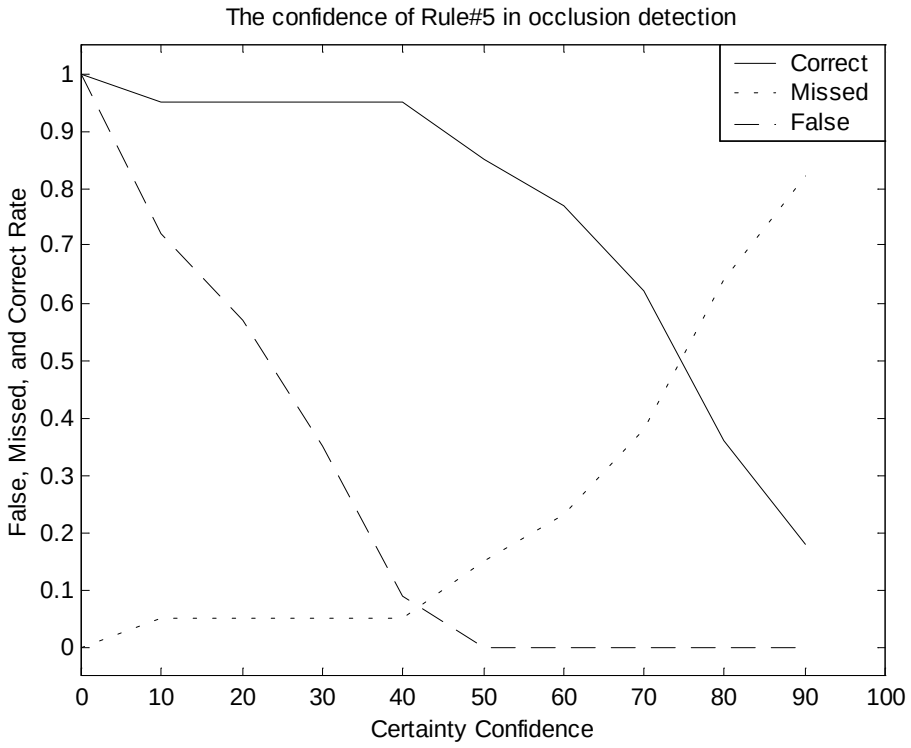

(a)

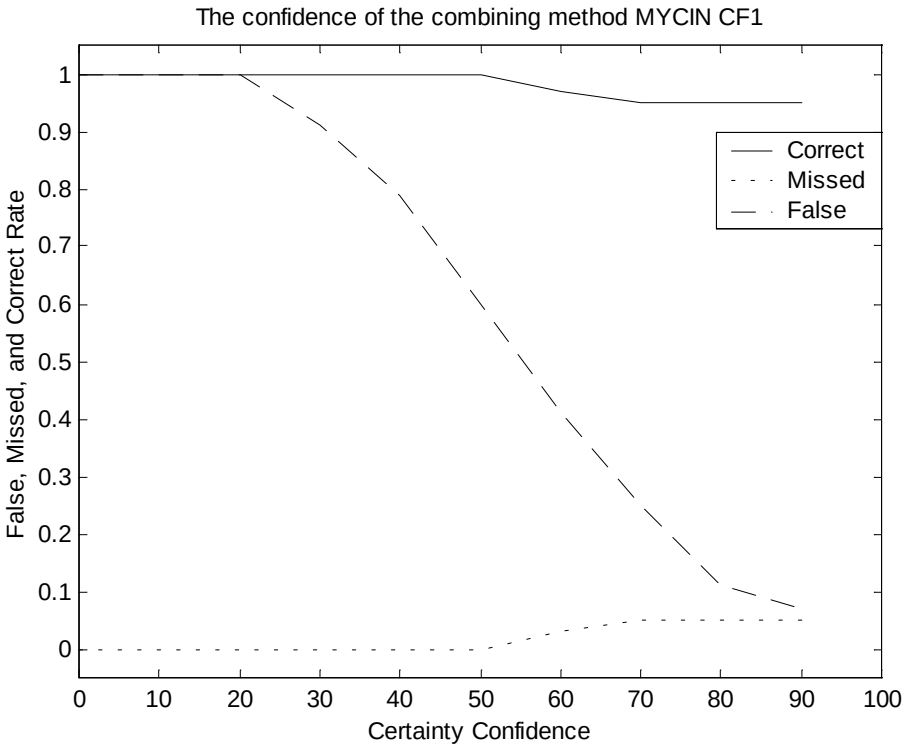

(b)

Figure 7.29 The certainty confidence for Rule #5 and the first combining method MYCIN's certainty factor. This is computed through measure of false, missed, and correct detection of occlusion at different certainties. (a) Rule#5. (b) MYCIN's certainty factor.

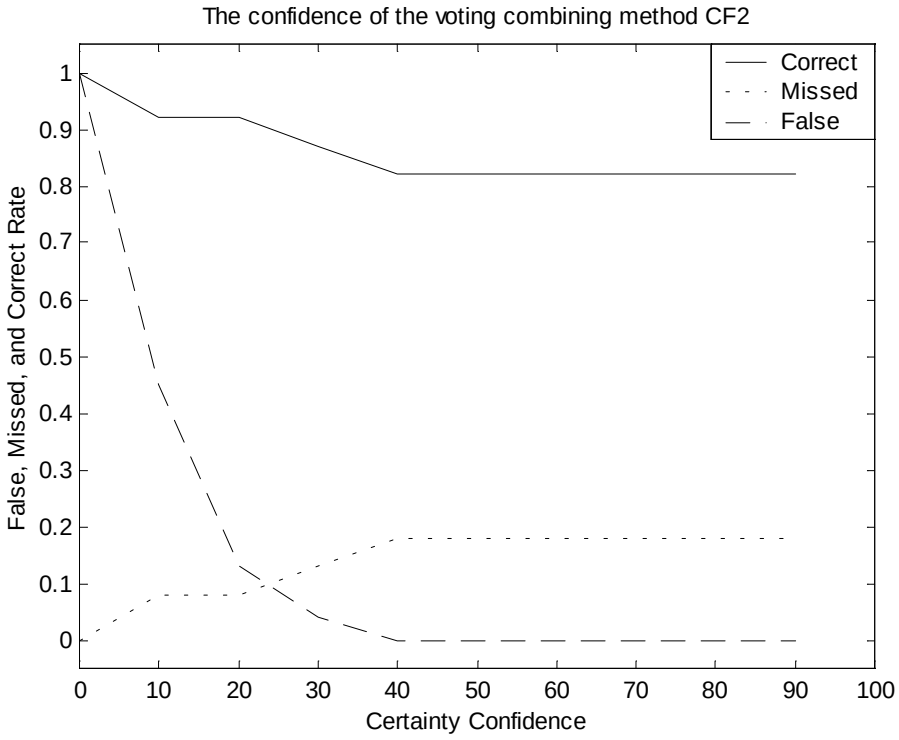

(a)

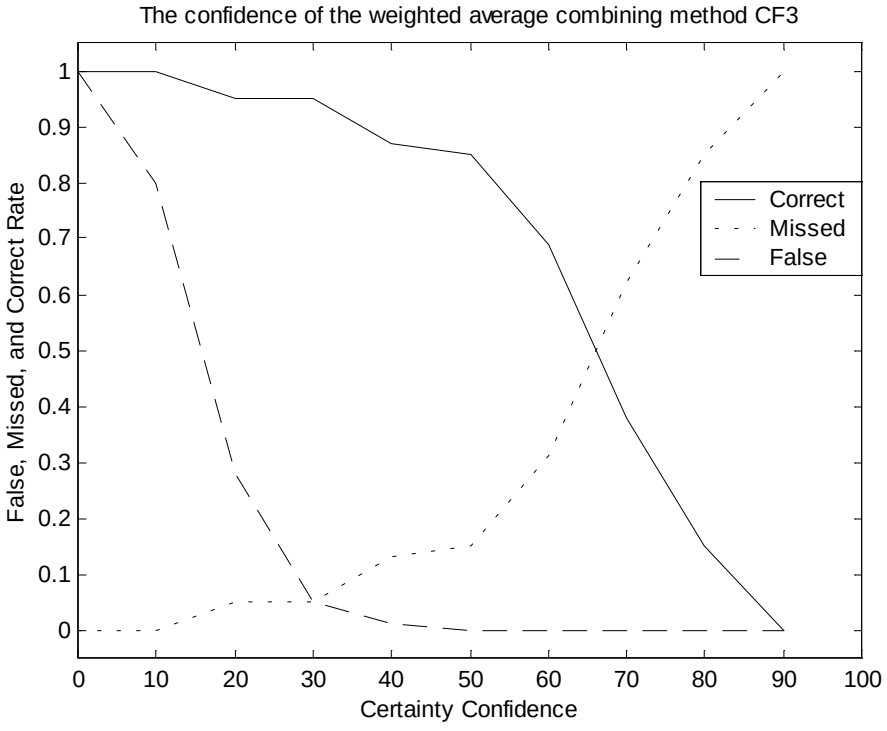

(b)

Figure 7.30 The certainty confidence for the second and third combining methods; voting method and weighted average method respectively. This is computed through measure of false, missed, and correct detection of occlusion at different certainties. (a) Voting method. (b) Weighted average method.

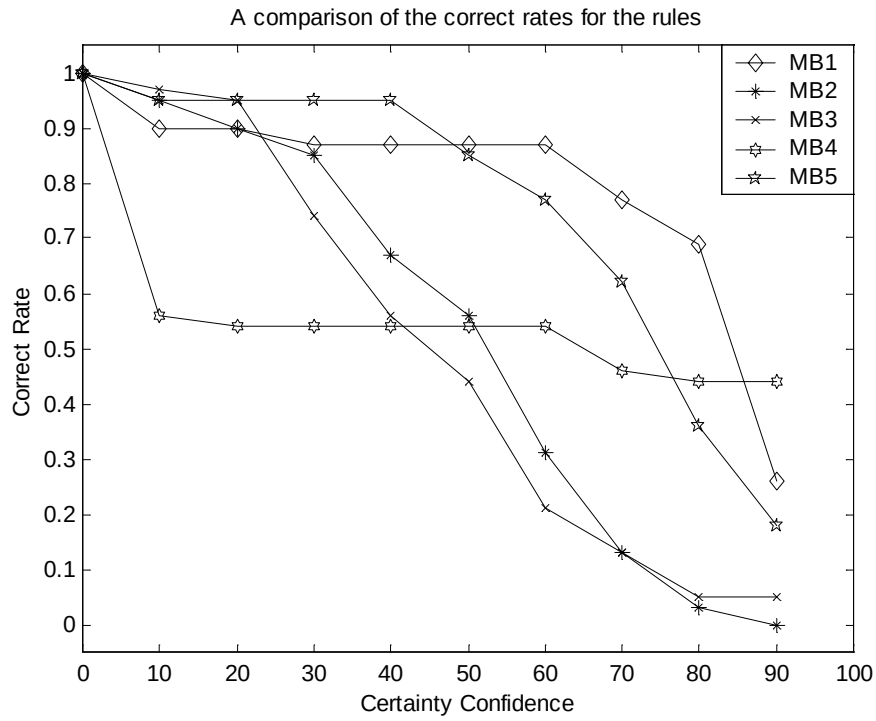

(a)

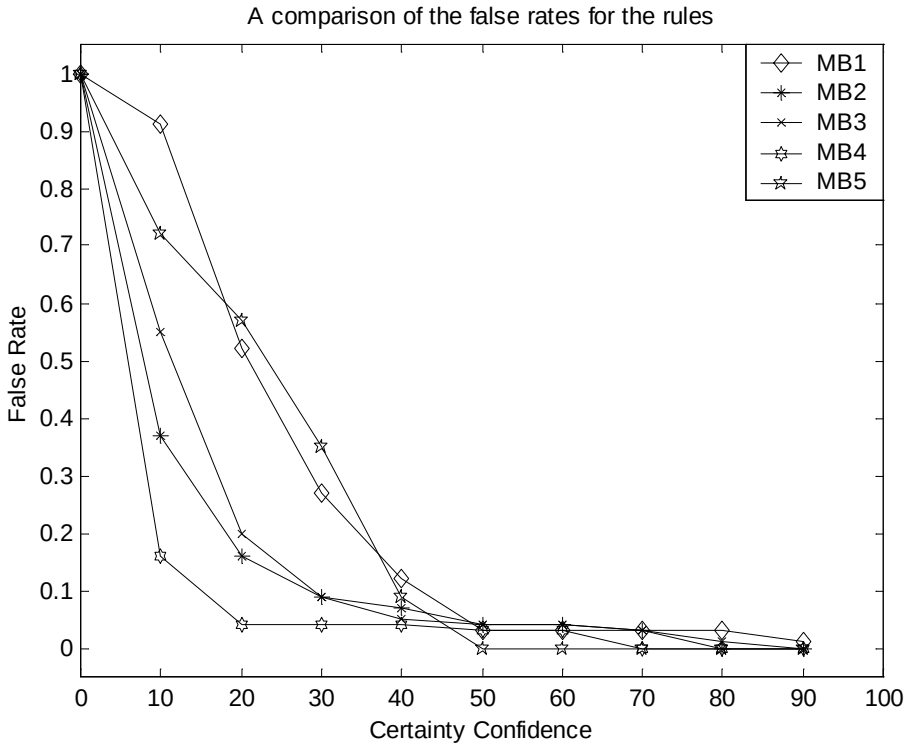

(b)

Figure 7.31 A comparison of the correct and false rates for the five rules at different certainties. (a) Correct rate. (b) False alarm rate.

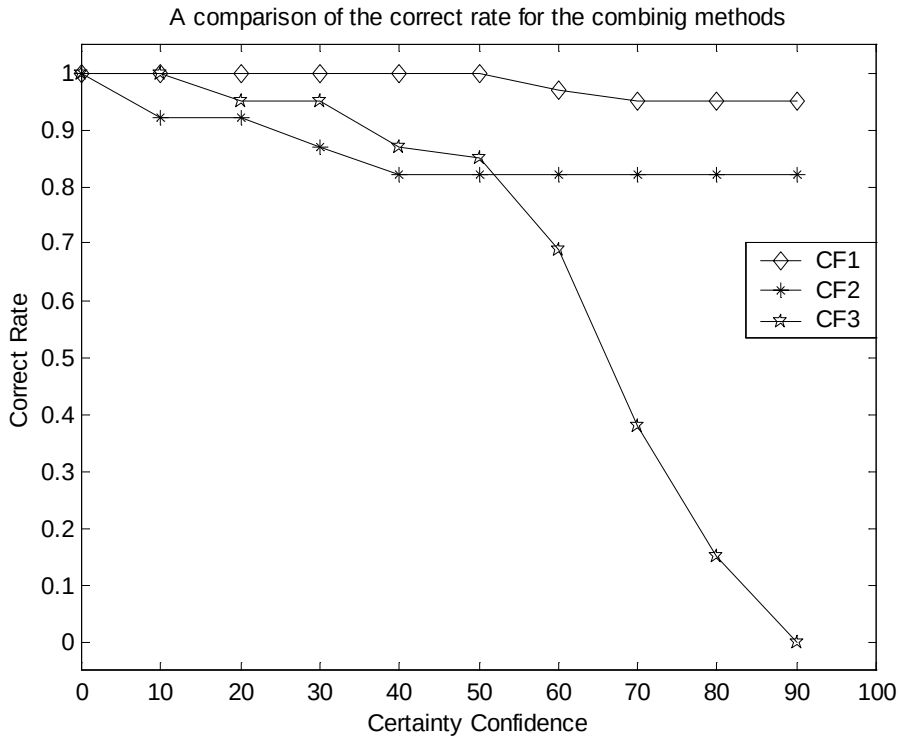

(a)

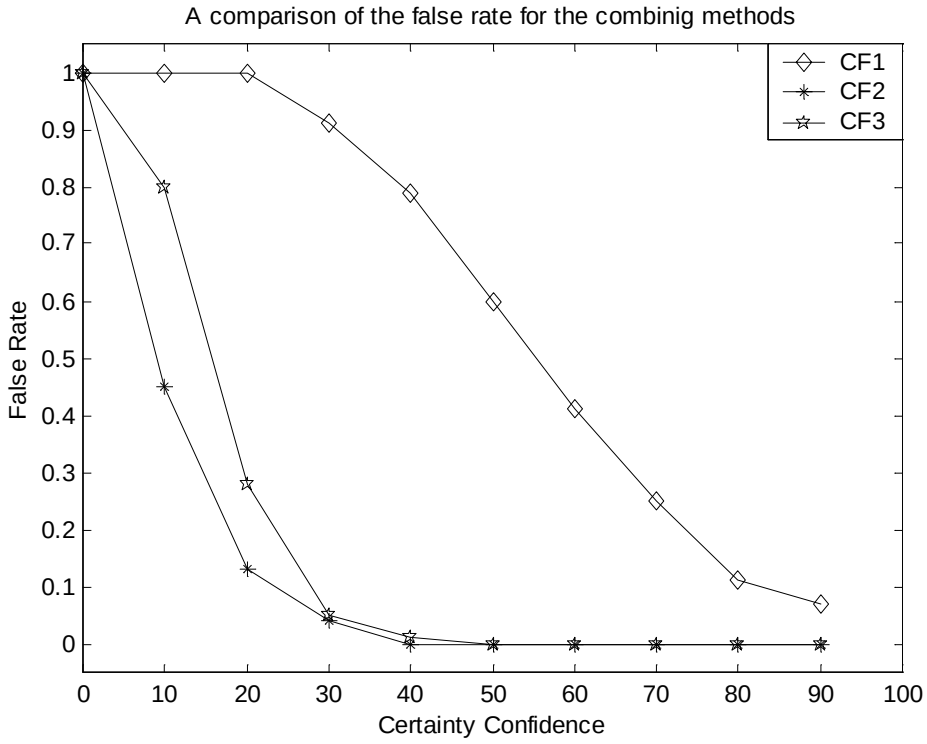

(b)

Figure 7.32 A comparison of the correct and false rates for the three combining methods at different certainties. (a) Correct rate. (b) False alarm rate.